Aerostructural Design and Analysis of a Wind Tunnel Model for Flutter Investigations

Jose Vicente Chardí Espí

September 18, 2018

POLITECNICO
MILANO 1863

DIPARTIMENTO DI
SCIENZE E TECNOLOGIE AEROSPAZIALI

Contents

List of Figures

List of Tables

Abstract

Exhaustive effort has been made by many different organizations to shine light and obtain valuable information in the field of aeroelasticity as a whole and also specifically in the domains of flutter and Active Flutter Suppression (AFS). FAA, as the main regulatory entity in the industry has been progressively taking steps towards the certification of AFS systems, by funding different research programs linked to these matters.

Under this umbrella, and in conjunction with the University of Washington, Seattle, DAER-POLIMI was asked to adapt an already available aeroelastic wind tunnel model to meet a set of pre-requisites, for posterior wind tunnel testing of a flutter suppression control law.

This thesis will serve to illustrate the process behind the design of the aero-structural elements required for the updating of the aeroservoelastic model, and the subsequent analysis to confirm the adequate performance of these components to grant the extrapolability of the results obtained during experimentation.

Acknowledgements

Before moving on, I would like to express my sincere gratitude to Professor Ricci for giving me the opportunity to participate with an active design role in the AFS project and for his constructive criticism. I would also like to specially thank Federico Fonte for his patient guidance and technical support throughout the development of this thesis, making the experience extremely enriching and allowing me to understand the insights of the design process behind a successful project. Also wish to thank the rest of the department members and individually Francesco Toffol for his time.

Furthermore I am immensely grateful for the motivation that my family has and will continue to generate in me thanks to their loving support.

1 Historical Background

Aeroelastic phenomena has been present in many aeronautical problems since the beggining of aviation. Many would even say that aerodynamic instabilities such as flutter, had caused havoc even before the Wright brothers managed the first ”heavier than air flight”. For example, [3] claims that Professor Samuel P. Langley might have been the first to suffer aerodynamic divergence, more precisely some form of wing torsional divergence, due to the wing's low structural stiffness that could be attained at the time. This issues lead to the adoption of bi planar wings (Figure 1b), which managed to delay flutter speed.

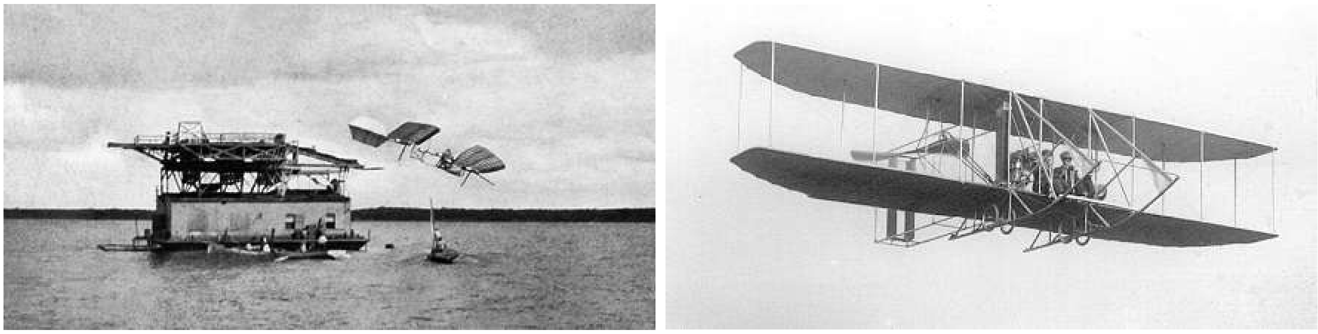

(a) Langley Aircraft

(b) Wright Aircraft

Figure 1: Origins of the Bi-Planar Wings

As commonly defined, aeroelasticity studies the mutual effect of both aerodynamic and elastic forces. The coupling between the aerodynamics and the structural deformation could progressively tend towards unstable operating points. Simply illustrated, a higher angle of attack would lead to a higher aerodynamic load which will in consequence cause a higher deformation of the intrinsically flexible structure, causing further rotation due to the non coincident elastic axis and the center of pressures, in turn resulting in an even greater angle of attack. This self-exciting behaviour could tend towards some equilibrium point, or contrarily induce the so called and feared divergence.

In the early stages of aviation, propulsive power was by no means exuberant and aircraft flew at relative low speeds, slow enough to remain below the loading conditions that could lead to instabilities. As power units were progressively developed, due to military needs, fighters started to suffer the effects of aeroelasticity. Biplanes granted enough torsional stiffness for the wings, but soon it was the tail section causing trouble. Nevertheless it wasn't until engineers started implementing monoplane wings due to their improved aerodynamic performance, that flutter affected main lift generating surfaces. These wings could withstand the maximum required loading factor in static condition with no problems, but engineers were baffled when they disintegrated in mid-air while in operation. A significant example of the impact that flutter had during World War I is the case of the Fokker D-8. Initially designed as a monoplane, it managed to serve in combat for only a couple days, as wings collapsed during the infamous high speed dives, costing the lives of the most experienced pilots (whom received the new units first) and could have had significant impact on the war's outcome.

Most of the mechanisms that might be described as aeroelastic must also deal with inertial forces due to their dynamic nature. Correspondingly flutter, as other phenomena such as buffeting or dynamic response depend on the three legs of the so called aeroelastic triangle of forces [8]. Axiomatically, engineers started using tools to characterize the dynamic response of structures, just as Lanchester and Bairstow used modal analysis to initially understand the tail torsional oscillations that were observed on the Handley Page 0/400 bomber.

Classical flutter, associated to potential flow, was understood as early as at the mid 30's. On the other hand, the much more complex non-classical flutter was a much greater issue as it was difficult to analyse from a theoretical point of view. This complexity, consequence of the number of flow regimes that could be involved in any particular scenario, led to a design process based on trial and error. Essentially flutter was fought by; either increasing the overall stiffness, mass redistribution to diminish coupling between natural vibrating modes or both, but no active counter measure was initially conceived.

2 Active Flutter Suppression (AFS)

Since control theory was developed and actuators met the performance requirements around the mid 60's, engineers have had the goal of mitigating if not totally cancelling the effects aeroelastic behaviour. Operating on the control surfaces allows to redistribute the aerodynamic loads, and adequate tuning of these deflections would allow to counteract the flutter just as noise cancelling devices cancel sound.

Even though great efforts have been made to design active flutter suppression, "AFS is still viewed with reservation and caution" [6]. While other control systems such as manoeuvre load alleviation, gust alleviation or even stability augmentation systems for unstable aircraft have been certified and widely used, AFS has been repeatedly held back by regulating institutions for precaution.

The aforementioned control systems have one key safety characteristic compared to AFS. In case of system failure the consequences would not necessarily be catastrophic as they would allow some chance for the crew to correct the attitude of the aircraft. On the other hand, active flutter suppression system failure could lead to fast appearance of divergence or even explosive flutter. The pilot would have no reaction time to respond adequately, and critical structural damage could lead to a fatal outcome. AFS to mitigate the effects of linear flutter has not yet been allowed on commercial aircraft and has had marginal application in the military industry [9] (B-1 bomber as an example).

On the other hand, current computational strength powering finite element software permits the understanding of the flutter mechanisms during the design stages. With this information and ensuring sufficient security margins, AFS could be closed-loop implemented to mitigate the non-critical modes, such as for example LCO's.

3 Flutter Wind Tunnel Experimentation and the X-DIA Aeroservoelastic Plant

3.1 Wind Tunnel Modelling

The combined challenge of dealing with coupled structural modes and the risks associated to the study of a flying plant while operating in unstable dynamics, make wind tunnel testing not only the most ”rapid, economical and accurate means of conducting aerodynamic research” [2], but also the safest.

Despite the advantage of working in a controlled environment, scaling between aircraft and model should be ensured or otherwise the results would not have applicability outside the lab, as the conditions would not have been equivalent to the ones the real aircraft would encounter during flight. For these matters, the dimensionless coefficients that compose the equations of motion in non-dimensional form should be preserved.

- $Reynolds = \frac{InertialForce}{VicousForce} = \frac{\rho V l}{\mu}$
- $Mach = \frac{InertiaForce}{ElasticForce} = \frac{V}{a}$
- $Froude = \sqrt{\frac{InertiaForce}{Gravity}} = \sqrt{\frac{V^2}{lg}}$

Usually Reynold’s and Mach are the parameters used to relate full size and scaled model, but in experiments where the dynamics play an important role, Froude becomes essential. Relating the parameters is achieved by modification of the flow conditions (ρ, V, T, P) in the wind tunnel test section, but other factors such as skin friction and rugosity, which are not easily scalable, will affect the flow and may vary the flow regime specially at boundary layer. In the specific case of wind tunnel tests with associated aeroelastic characteristics, even more restrictions should be imposed as the vibration modes, natural frequencies and intrinsic stiffness of the model should also be faithful to the full scaled version.

Alternatively, conceiving a completely independent experimental plan, which would eliminate these scaling issues and reducing cost, could still be useful if its behaviour was representative of a "typical aircraft" describing the model segment to study.

Arranged to match an objective scaling factor of 1/10 in all, dimensions, weights and moments of inertia with respect to the "typical aircraft" the X-DIA was conceived as a Research Remote Piloted Vehicle (RRPV) experimental plant for both aeroservoelasticity and flight mechanics experiments. Owing to the scientific debate at the time (1995), discussing the superiority of unconventional configuration, the model was conceived to test two canard configurations, forward and backward, and their implications in trimming.

In most aeroelastic experiments it is common practice to use a vertical rod mount as the one seen in Section 4.6.2 which also allowed roll, however for these experiments the X-DIA will be hung using a cable bridle to center the model in the tunnel and allows for the full aeroservoelastic nature to be studied.

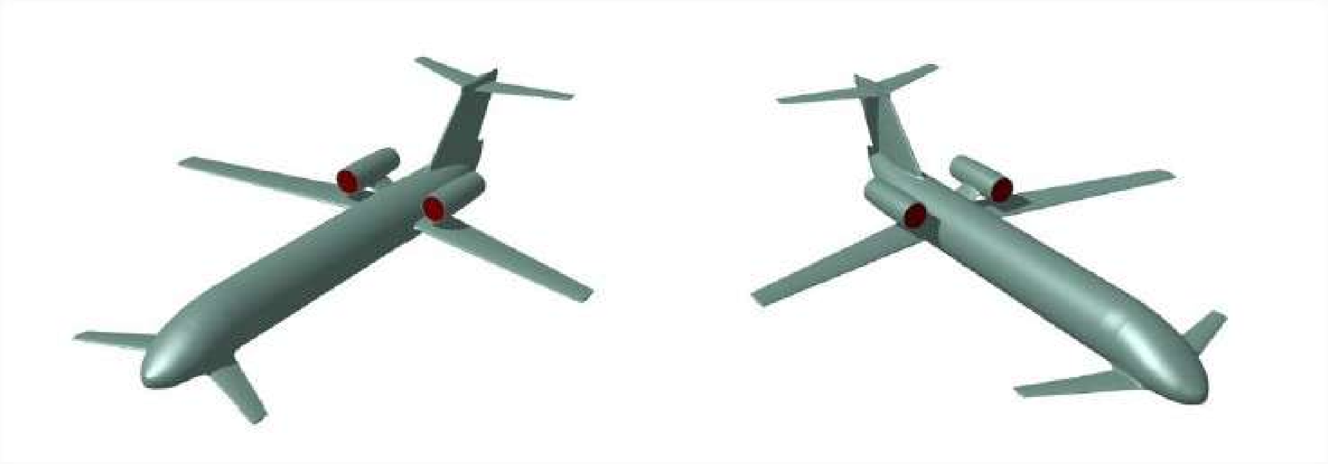

Figure 2: X-DIA wind tunnel model conceive for 3AS project

The wind tunnel testing was to be held at the Large Wind Tunnel of Politecnico di Milano, a low speed facility with a maximum $V_\infty = 55m/s$. Due to the low range of velocities at which the model would have to operate it was Froude's Number the dimensionless parameter that was fixed.$Fr^2 = \frac{v}{g*l}$

3.2 Flutter Analysis of Original X-DIA Configuration

Once the stability and stability margins of the model were confirmed, it was important to understand the way in which flutter would appear during the experimental research. Visualizing the flutter modes would help discern how the full model would behave. Eigenvalues provide information about the flutter speed while the eigenvectors are useful to study how the plant deforms providing information as to how it should be modified to correct undesired attitudes.

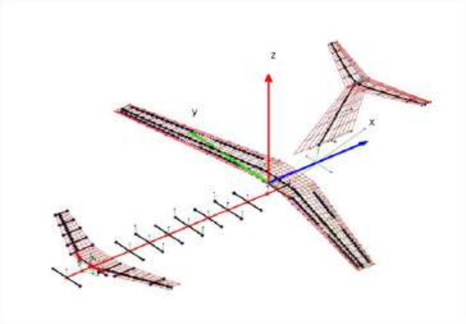

Figure 3: X-DIA Structural and Aerodynamical Model

A flutter analysis was performed on the configuration with backwards canard (Figure 3). So as to simplify the computation, the full model was reduced by discretization to a combination of nodes representing the aircraft's morphology. In order to correlate the aerodynamics with the structural model, splines were placed linking the aero-panels (NATRAN's description of lifting surfaces) with the discretizing nodes of either wing spar o tail spars. This order reduction had the advantage of greatly simplifying the simulation while still being representative of the actual expected behaviour of the plant's deformations and modes.

From the results, the team rapidly identified the coupling between rigid body motion and elastic modes. As in any other aeroelastic phenomenon, the mechanisms manifestation are a consequence of not only the mass distribution but also of the aerodynamic loading and hence the aerodynamic architecture.

The mentioned coupling implied that the flutter mechanisms were more complex in nature and inevitably the characterization of the aero-structure behaviour would be more challenging. In combination with the fact that the results obtained using a less traditional configuration could in turn be less extrapolative for general use, and as to fulfil one of the project's premisses of simplicity, it was decided to return towards a more traditional frame and make the model more manageable.

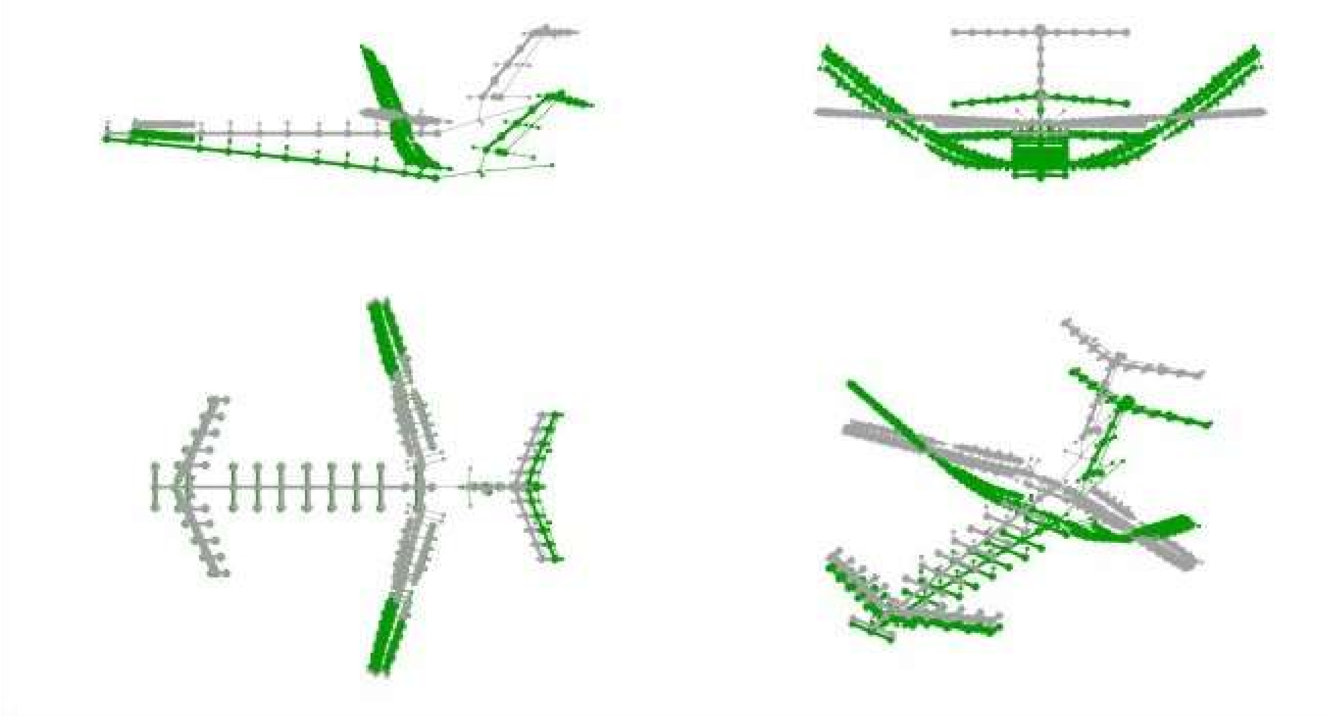

(a) X-DIA Flutter Modes

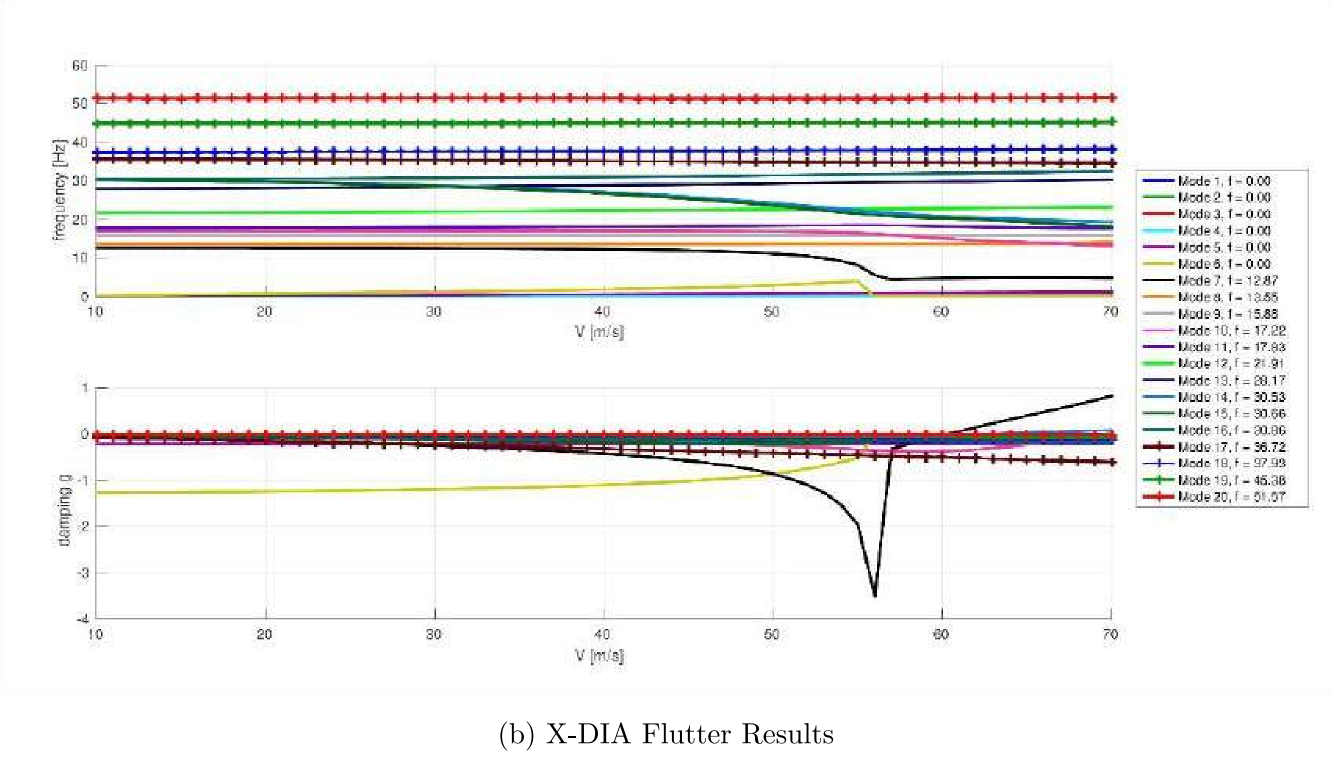

(b) X-DIA Flutter Results

Figure 4: X-DIA Flutter Analysis

3.3 Modification of X-DIA and Flutter Analysis of New Architecture

The X-DIA was reconfigured to substitute the negative sweep in favour of a more traditional and convenient sweep while the canard was simply removed. After the modifications, the scaled plant had a much greater resemblance to a typical commercial aircraft but the frequency response would still have to be determined.

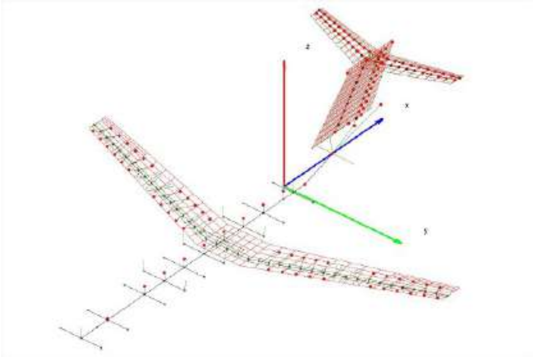

Figure 5: Modified X-DIA Structure for AFS project

Following the same procedure, a second analysis was performed on the newly modified X-DIA. This time the coupling between the rigid and elastic modes was significantly lower, so by modification of the model architecture, the plant had become more controllable.

Unfortunately, the results concluded that the flutter speed ($V_{flutter}$) was around $69 m/s$, associated to mode 7. This V_∞ is beyond that attainable at POLIMI's facilities and hence not practical. Consequently it was imperative to design some counter measure to decrease the speed at which flutter would appear.

In [1] a parametric study to investigate the effect that, introducing concentrated masses, at different chord percentages of the wing-tip section would have on the flutter velocity, was conducted. This work concluded that small masses, specially when placed towards the trailing edge, would have great impact on $V_{flutter}$ causing it to decrease into the wind tunnel's range.

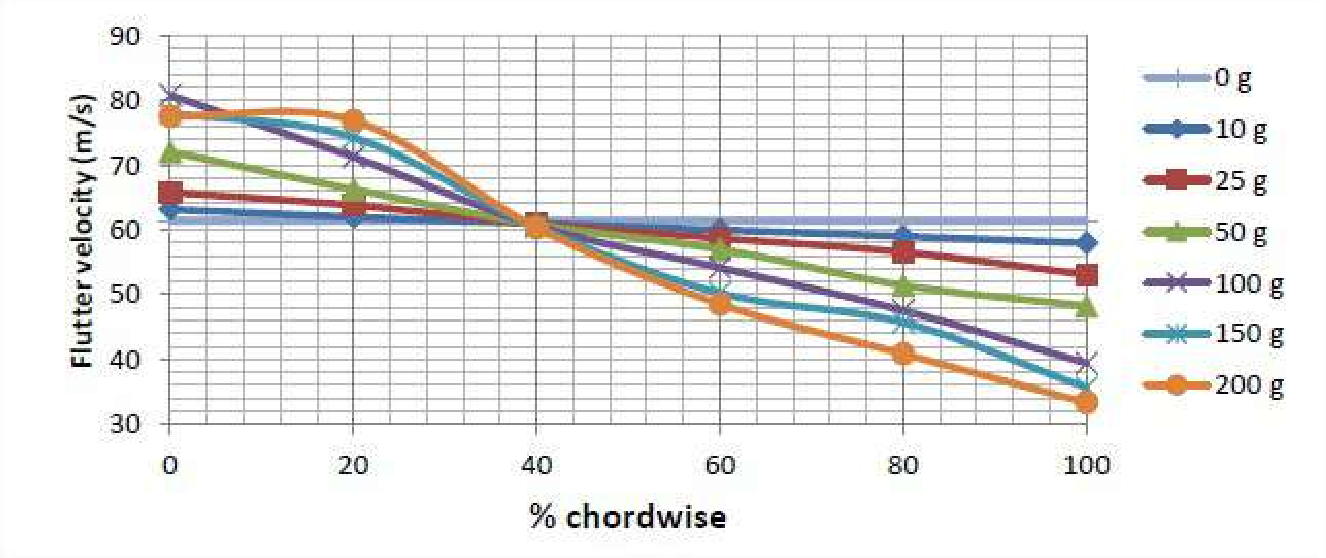

Figure 6: Flutter velocity depending on the lumped mass added at tip variation

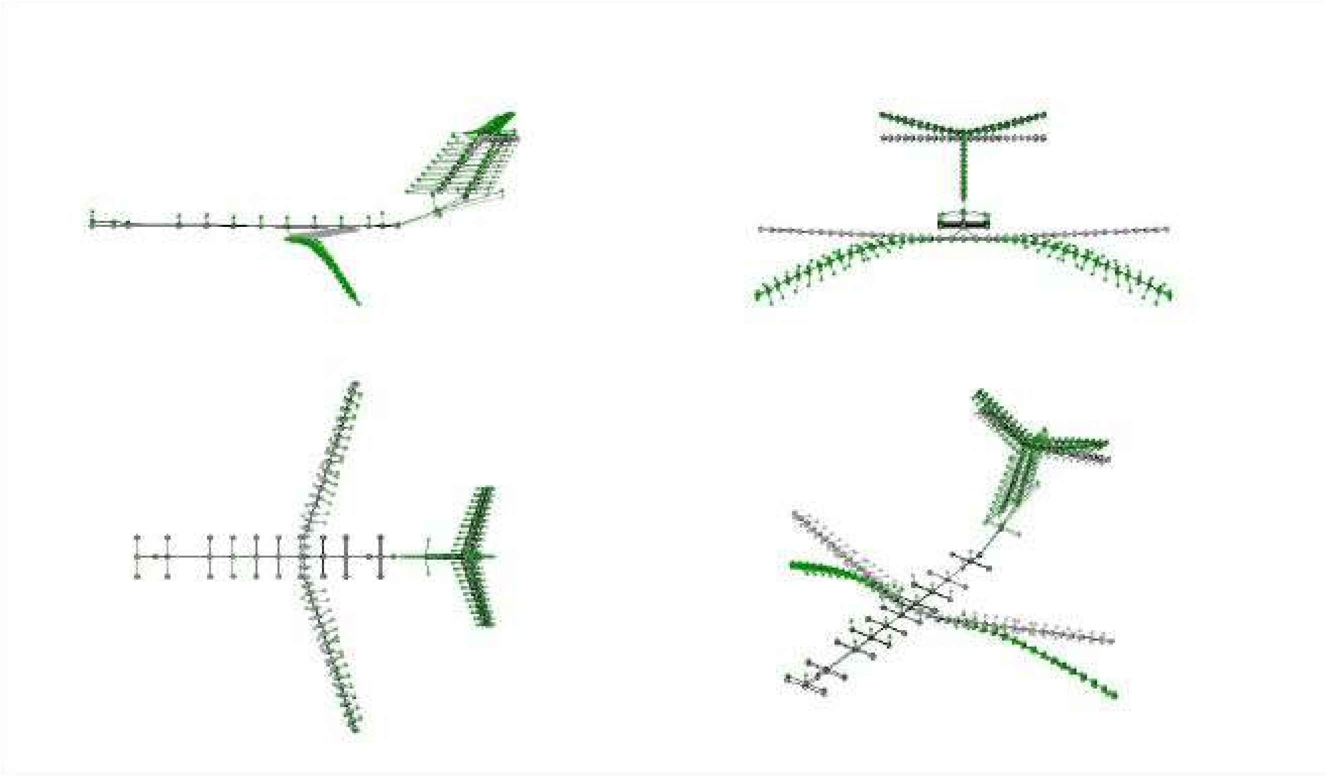

(a) X-DIA MOD Flutter Modes

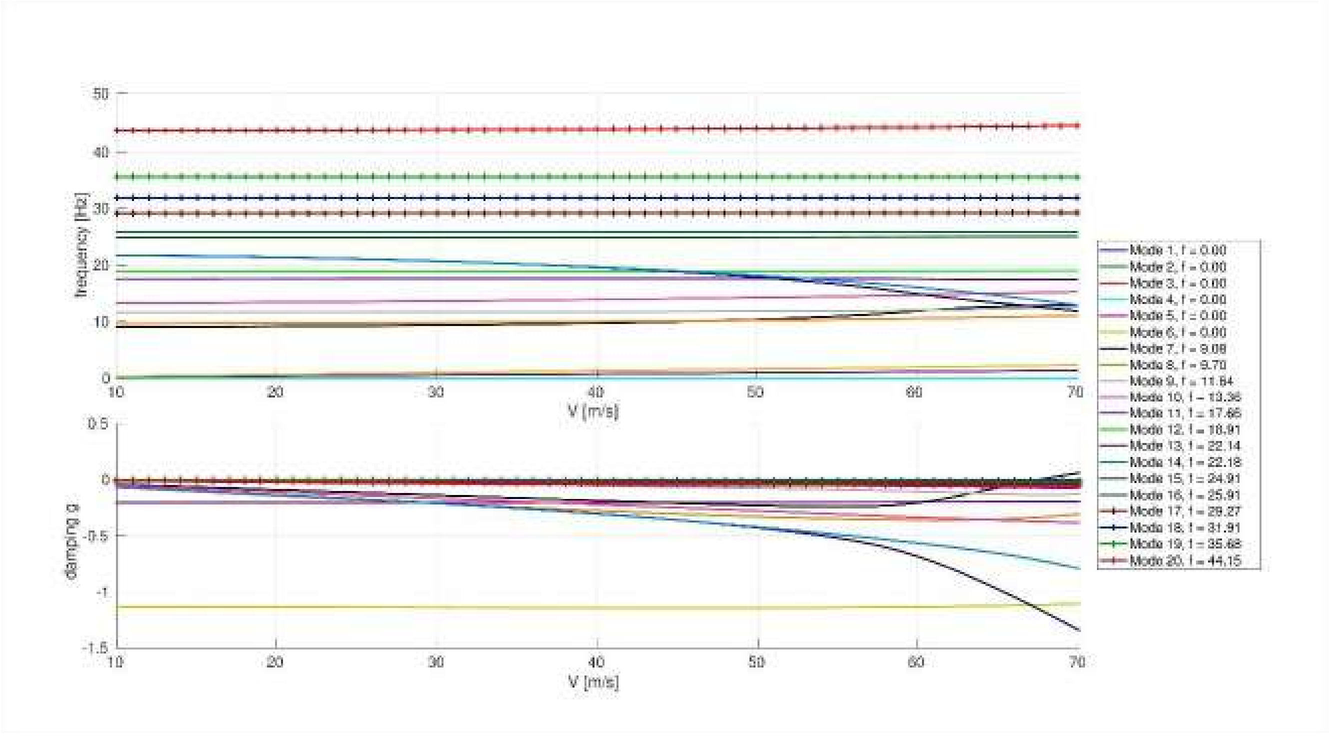

(b) X-DIA MOD Flutter Results

Figure 7: X-DIA Flutter Analysis

4 Structural Design of Main Assemblies

4.1 Discernment of Re-Usable Structural Elements from the Original X-DIA Plant

Before starting the development of the assembling components, it was required to elucidate which components could be re-used and which would have to be designed. The fuselage beam (core of the model) and the fuselage aerodynamic sectors had been conceived in a manner that made them extremely versatile.

4.1.1 Fuselage Beam

The beam is defined by a rectangular section of dimensions $80x50mm$. As the main longitudinal structural element it spans from nose to tail with a length of 2140 mm. The fact that it was made from an aluminium alloy, Aluminium 2011 T3 more precisely, and it's hollow section (3 mm thickness) makes the beam very efficient if we talk about mechanical strength to weight ratio.

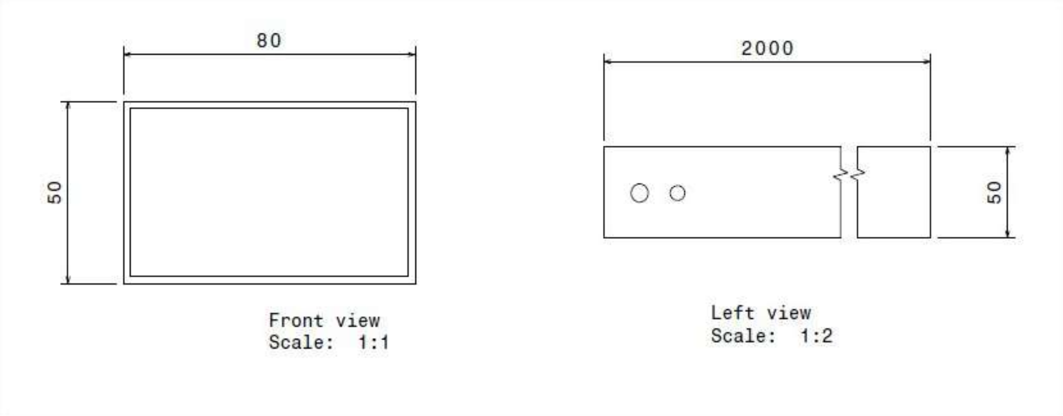

Figure 8: Fuselage Beam Dimensions

Table 1: Aluminium 2011 T3 Characteristics

Material	Density ρ (kg/m^3)	Young Modulus (E) (units)
Aluminium 2011 T3	2823,402	7,0327E+10

These properties make this type of aluminium beam very interesting for this project specifically but also relevant for aero-structures in general. Fundamentally, the beam may be considered as the cornerstone of the X-DIA internal structure, and despite being the main structural reference it only accounts for 3,045 kg of the total weight.

4.1.2 Fuselage Aerodynamic Sectors

The X-DIA fuselage had been designed and manufactured divided into a number of aerodynamic sectors while each one of these sectors was in turn formed by two sub-elements that once assembled completed the circular section of the fuselage. Figure 9a

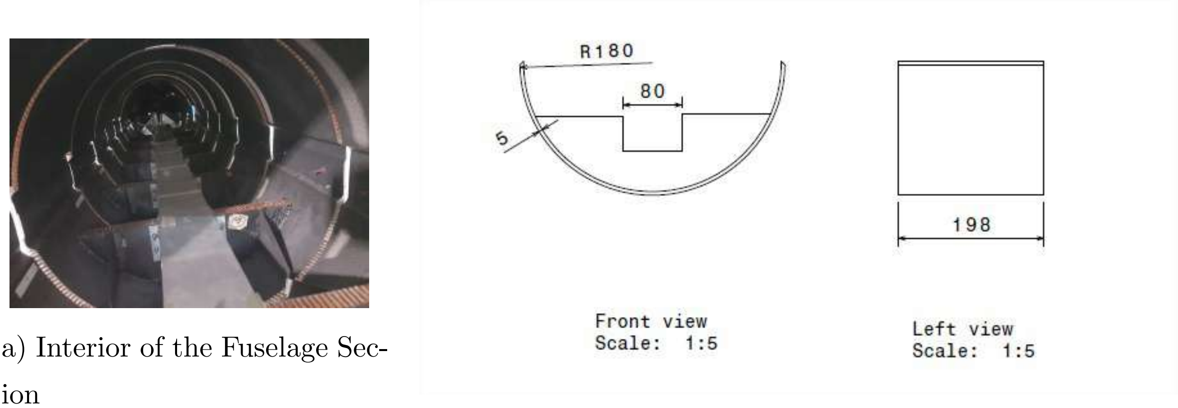

(a) Interior of the Fuselage Section

(b) Fuselage Sectors Dimensions

Figure 9: Fuselage Sectors

As J.R.Vinson illustrates in [7] a typical sandwich configuration, like the one used for the fuselage, has 300 times the flexural stiffness of the equivalent monocoque construction. Furthermore it will work better under loads associated to buckling, even though buckling will most probably not happen within this model due to the discretization of the elements into sectors. The conclusion to be drawn from this is that the fuselage deformation, if any, will be due to the beam's elastic compliance exclusively.

Subdividing the sectors had its main reason associated to the fact that gaps in the structure had to remain in order to allow the aeroelastic behaviour to manifest itself with ease. Direct contact between sections would increase the rigidity of the model and hence would shift the natural modes towards higher frequency ranges, frequencies that might not be achievable in a low speed facility.

Furthermore subdividing also yielded an advantage in terms of manufacturing. Manufacturing a single cylinder in composite material would greatly increase the cost, as such a part would probably need to be cured inside an autoclave oven. Simpler, shorter elements would be manufactured with greater ease and hence the budget could shrink.

This implementation also made the model very versatile allowing for untroublesome reconfiguration to match a vast number possibilities. In the original design, the wing, with negative sweep angle, was mounted from behind the rear section of the fuselage (nearest fuselage sector in Figure 10a) and it was at this point where the tail cone originated. After modification, the wings were moved forwards along the fuselage beam axis and hence some fuselage sectors had to be re-positioned. If the fuselage had been designed as a single cylinder, then major modifications would have had to be tackled, again increasing the overall cost of the project.

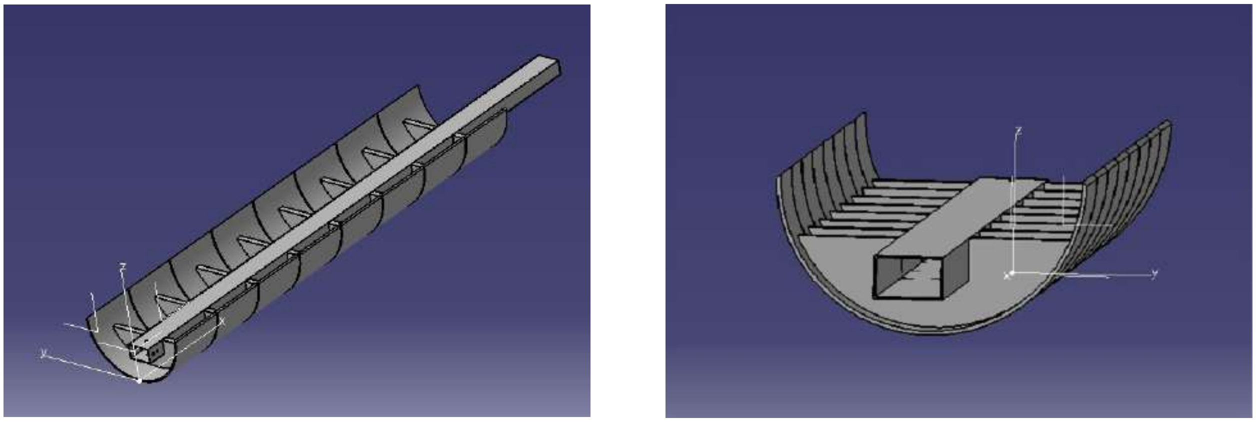

(a) (b)

Figure 10: Fuselage Mounted on Fuselage Beam

4.1.3 Wing Spar

The old wing spar had been milled from a block of the same aluminium alloy as the fuselage beam, hence sharing its intrinsic characteristics. Despite the CNC machining, the CAD file was not available and measurements had to be taken in situ. Generating the ".part" from lab measurements had the risk of introducing both measurement and fabrication errors into the design process, but due to the slenderness of the spar, these deviation would most probably fall in the range of manufacturing tolerances and may not be regarded as critical.

Figure 11: Picture of the wing spar

From Figure 11 it is important to note how the spar's axis is straight and normal to the wingtip spar section plane. Contrarily the root section is cut to match V_{wind} direction. These two planes are at 15° the one respect to the other as it is stands out in Figure 11.

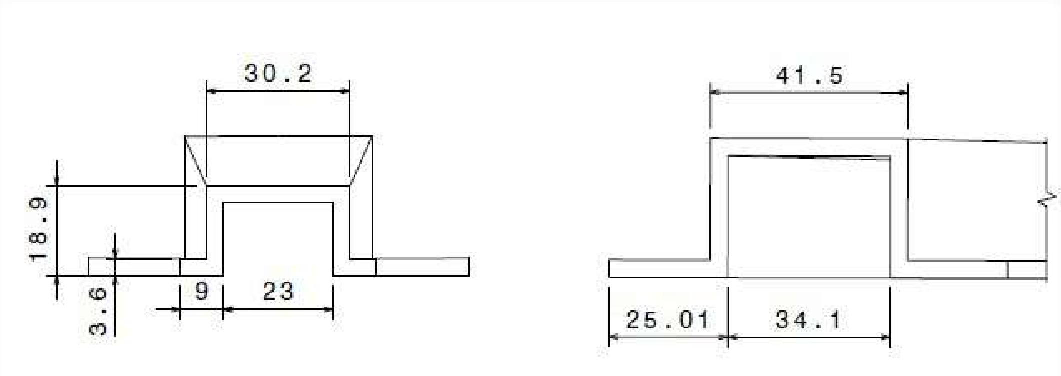

Figure 12: Omega Shaped Sections

The main characteristic of the wing spar is the "Omega" shaped section. As in the "I" beam, the web, in this case the two vertical plates, withstand the out of plane bending, while the flanges will work in the plane. This shape allowed to easily dimension root and tip sections to match desired sectional stiffness, and the linear interpolation that describes the longitudinal evolution of the geometry would set the stiffness as a function of a coordinate aligned with the spar's elastic axis. It should also be noted that as consequence of being an open section, it would be more sensitive to torsional loads, so was the case that enforcements were introduced, closing the section at some specific regions, to increase the characteristic torsional inertia of the spar.

The omega shape is also useful in terms of assembling a wing on it, as the two lateral flanges serve as an ideal support upon which to fasten the aerodynamic sectors (further described in section 4.2.1).

4.2 Aerodynamic Configuration of the X-DIA

4.2.1 Wing Sectors

Given that the spar's geometry was fixed beforehand, it was interesting to research the availability of aerodynamic profiles that would allow sufficient space for the spar. A profile with flat lower part would be ideal due to the planarity of the bottom of the spar. Different candidates were studied by comparing their aerodynamic characteristics and their geometries. The Eppler series seemed to meet many of the requirements, and among them, the "e582" was selected.

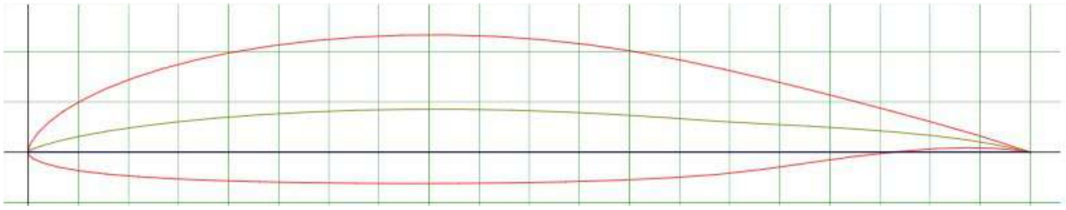

(a) "e582" Aerodynamic Profile

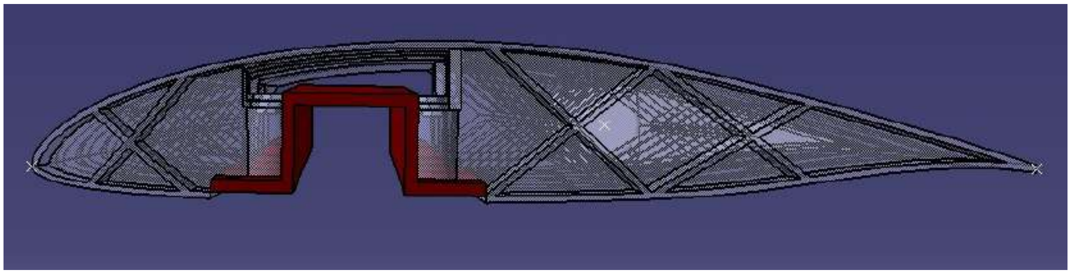

Figure 13: Positioned Spar, Bolting Pillars and Wiring Channels

Furthermore, the design was developed bearing in mind that the parts would be 3D printed. The main advantage of the additive process is that it allows to form geometrically complex parts, both internally and externally, capable of adequate interaction in assembling situations. This technique allows the introduction of structural elements and bolting geometry in a way that no other manufacturing technique could. For example, after positioning the wing spar, pillars for both support and bolting were introduced directly attached to the rib plane and hence forming part of the sector's bodies themselves.

3D printing also allowed to form the stiffening internal pattern. Despite not being dramatically complex, no other technique would have allowed this kind of internal hollowing. In consequence sectors could be designed with sufficient rigidity, while keeping the overall mass low enough for aeronautical projects.

Lastly it should be noted how the wing sectors were designed to ”sit” on the wing spar. Once positioned they would be secured in place by means of two bolts connecting the 3D printed geometry to the wing spar. Due to the discretization of the wing and the mentioned sitting interaction, any sector could be unassembled individually. For this reason it was decided to allow a gap above the omega shaped spar so that cabling for sensors and actuators could be easily accessed when required, allowing for convenient maintenance. Figure **??**

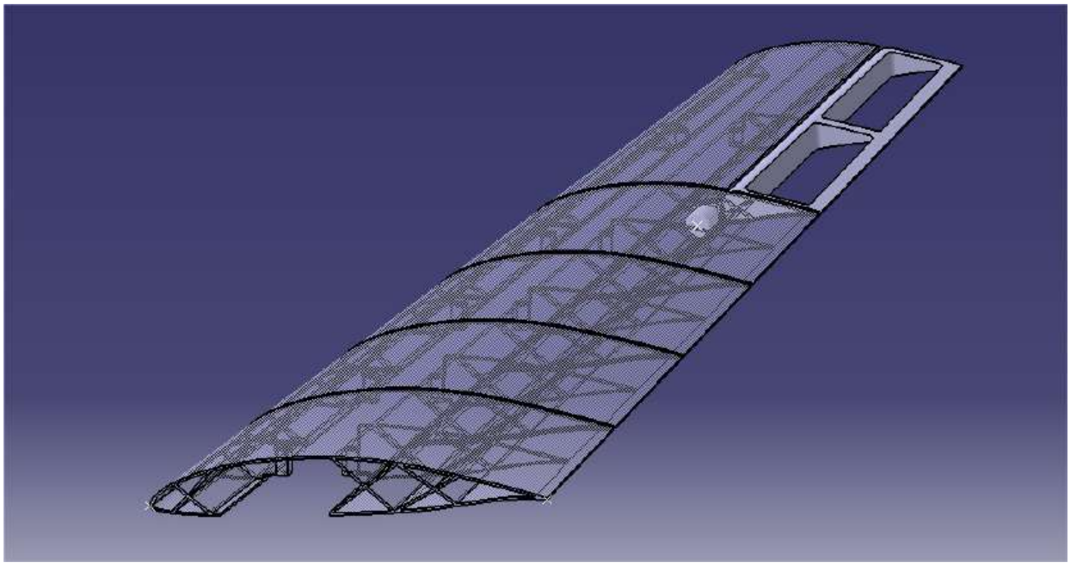

Figure 14: Wing Sectors

4.2.2 Tail

The geometry describing the tail's aerodynamics was also available from the beginning of this design experience. Following from the previous projects, the tail was once again designed using the well known "T-tail"and used in [4]. This design places the tail horizontal plane above the disturbed flow in cruise conditions and in consequence will be less perturbed, yielding a higher efficiency. Obviously in high angle of attack situation the control and stabilizing surfaces interact directly with the slip stream and could cause serious stalling, nevertheless this situation will not happen in the wind tunnel and the disadvantages of "T-tail"configuration would not cause great impact.

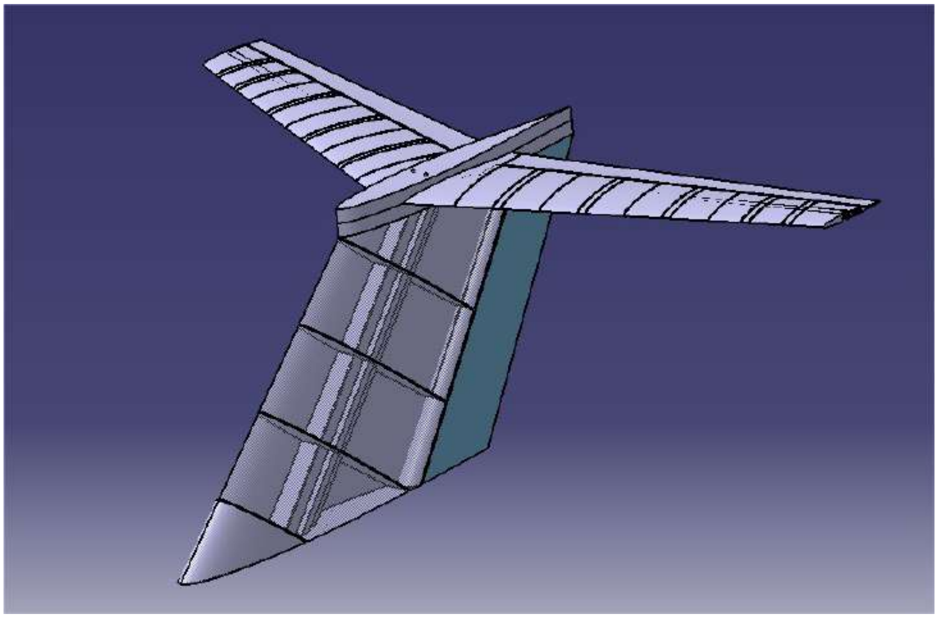

Figure 15: Tail Configuration

As seen in the preceding sections 4.1.2 and 4.2.1 the aeroelastic mechanisms should be allowed to manifest themselves and once again gaps between sectors were introduced. Exploiting the capabilities of sandwich composites the tail was manufactured with a foam core and carbon fibre, resulting in an elements with high flexural stiffness.

Split along the longitudinal symmetry plane, the tail was divided into building blocks. Each section is conformed by two aerodynamic shells enclosing the central vertical tail spar. The trailing edge of this vertical portion of the tail is completed by the rudder, which runs almost the entire length. The aerodynamic blocks would be mounted from the lateral allowing for simple mounting and dismounting of individual units if required just as what was conceived for the wing sectors, again making the tail easy to manipulate.

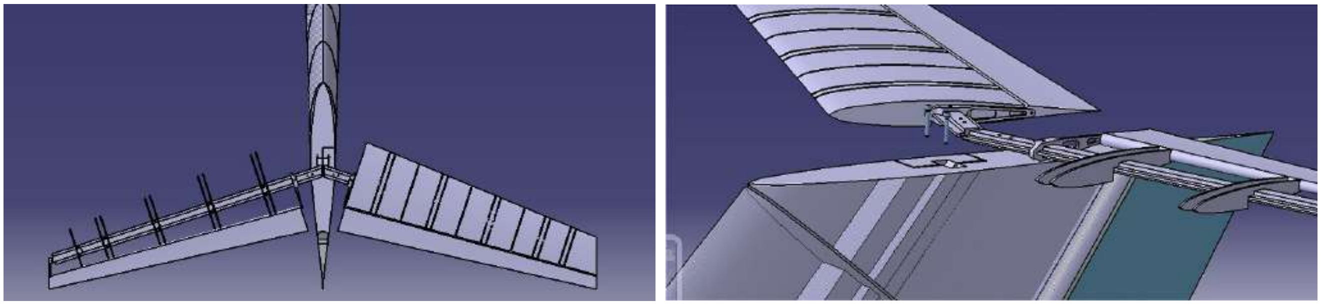
(a) Tail Plane Top View (b) Interior Tail Structure

Figure 16: Tail Structural Components

Finally, to complete the empennage the horizontal stabilizing surfaces diverge from the central column sustained by two more spars, as seen on Figure 16a and Figure 16b. Due to the slenderness of both horizontal tail spars and horizontal stabilizer aerodynamic sectors, some ribs in the form of plates were introduced to sustain the sectors in positions and are the ones in charge of transferring the aerodynamic loads into the structure through the tail spar.

4.3 Requirements for the Components to Design

Once the components that could be re-used had been selected and the positioning of the aerodynamics was clear, it was a matter of designing the assembling elements.

As in any other design project, there were several premises to fulfil. In this particular case, dealing with both static loads and dynamic behaviour the requisites had to be doubly enforced. Below is a list with the main concepts that had to be granted during the design phase:

- Weight: Crucial in any aeronautical project, the best way to reduce the weight will be to simplify the geometries to the maximum. This may be achieved by the use of adequate materials with high strength to weight ratio.
- Rigidity: Direct consequence of the aeroelastic nature of the experiment. Despite having the need to study flutter, this behaviour would be induced by the flexing of the wing and tail spars, the connections should not have a great impact on the overall behaviour of the plant.
- Ease to Assemble: Making assembling easy will inevitably make disassembling simpler. As a consequence it will facilitate substitution of damaged parts or access to the model's nervous system.
- Versatility: Modular design with the combination of non-unique positioning of parts would make the scaled X-DIA extremely versatile allowing it to morph into different configurations and could be used to validate a wide spectrum of aircraft.
- Manufacturability: Every single part should be deigned bearing in mind the technique that would be used to manufacture it. Studying beforehand what can or cannot be produced, given a specific technique, would save time and in consequence money.

4.4 Relative Positioning of Provided Aerodynamics to Match the Neo-Cass Model

Once all previously available parts had been digitalized to be used in CATIA V5, it was vital to adequately position all elements before jumping into the task of assembling them together. Using the NEOCass model and the Matlab plotting interface to extract certain reference points, a simple script was coded to obtain the relative positioning of the main aerodynamic elements.

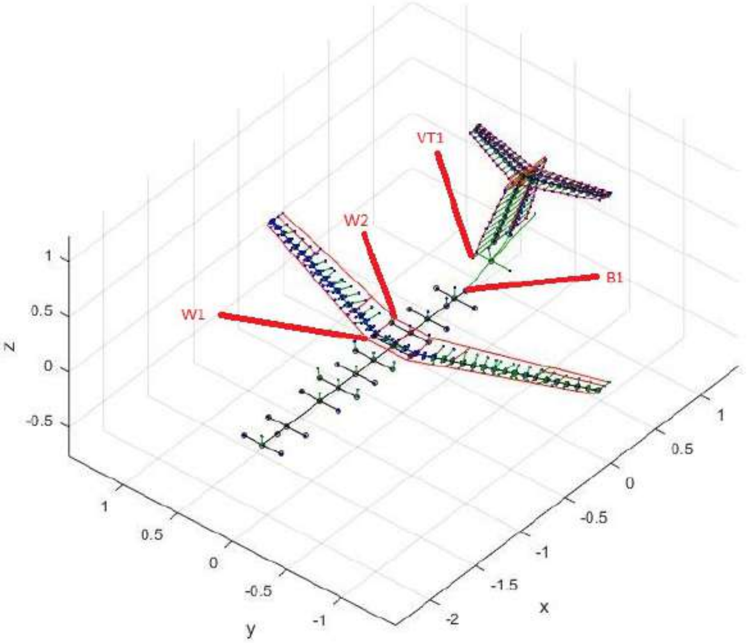

Figure 17: Matlab Plot of X-DIA with reference points

Table 2: Reference Points For Positioning

Point	Description	x-coordinate [m]	y-coordinate [m]	z-coordinate [m]
B1	Beam edge	0.2068	0.0000	-0.0950
W1	wing leading edge (root)	-0.6660	0.1800	-0.0900
W2	wing trailing edge (root)	-0.3587	0.1800	-0.0900
VT1	Vertical tail leading edge (root)	0.2805	0.0000	0.1492

After the reference points in cartesian coordinates x, y, z were extracted using the Matlab plotting interface, they were stored as constants with whom to calculate relative distances. These dimensions were calculated in vectorial form as that would help pose much simpler constraints in the CAD assembly. By the extraction of three points, apart from the beam edge coordinate and introducing angle constraints between components, all aerodynamic surfaces had been successfully positioned.

Table 3: Relative Distances Between Aerodynamic Components

Name	Description	x-component [m]	y-component [m]	z-component [m]
D1	distance between end of beam and wing leading edge	-0.8728	0.1800	0.0050
D2	distance between end of beam and wing trailing edge	-0.5655	0.1800	0.0050
D3	distance between end of beam and v-tail leading edge	0.0737	0.0000	0.2442

Visualizing the relative position of the main components was enlightening as it made self evident what type of connection should be designed and what elements could be discarded as redundant beforehand. This inevitably takes the engineer a step closer to the optimized solution and greatly reduces the time consuming iterative process required to obtain the best structure possible. A simpler solution will obviously be cheaper and would also be less prone to malfunctioning.

4.5 Wing to Fuselage Connection

The main requirements of the connection were to ensure sufficient rigidity as the wings would be the most affected by flutter, while allowing for some versatility. A clamp like structure was the best solution as it would allow a rugged connection. The clamp was formed by two independent parts that would enclosed the beam and would be tightened by means of bolts. Two more bolts, connecting both clamps and the fuselage beam would avoid the sliding of the assembly so that the wings could remain fixed at the desired distance along the fuselage beam.

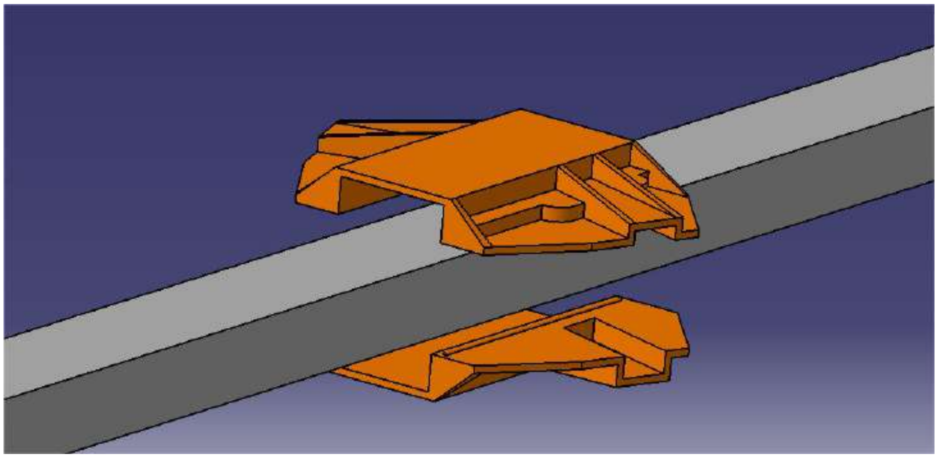

Figure 18: Shell Clamping Around Fuselage Beam

This set-up was interesting because it permitted the movement of the wing position forwards or backwards with great ease, hence allowing for some trimming if needed and its versatility could make it useful for future configurations with different wing positioning.

The wing spar itself, due to its omega shape allowed for a very simple and robust connection by means of an insert that would fit inside the inner cavity formed by the section. Initially a first design was produced with the aims of allowing for some sweep angle variation, and hence some aerodynamic morphing, but it soon became evident that this concept would be the weakest part in the assembly. Its intrinsic weakness would cause the wing's vibrational frequencies to decrease, probably inducing flutter at an excessively low V_∞, or even allowing the spar to rotate instead of deforming (only the insert flexes).

Consequently a new version was designed exploiting the robust nature of the insert section that would fit inside the wing spar. This more robust section was extended following the insert axis, and the shell clamp geometry was modified to meet the requirements. A newly conceived cavity would clamp the new insert in position as seen on Figure 18.

The insert geometry was designed to transform both the dihedral and incidence angle of the profile into neutral angles. This explains the torsion appreciated in both Figure 19a and Figure 19b. The reason behind this decision was to simplify to the maximum the two clamping shells, as any out of plane machining would inevitably lead to more complicated manufacturing and in consequence higher production costs.

Due to the planarity of the clamps mid-plane, it was important to ensure that the shells would not become excessively compliant to bending, as the insert would introduce loading in the normal direction to the plane. By introducing nerves, at leading and trailing edges as well as at the region destined to clamp the insert, the connection was made stiffer to behold the introduced forces.

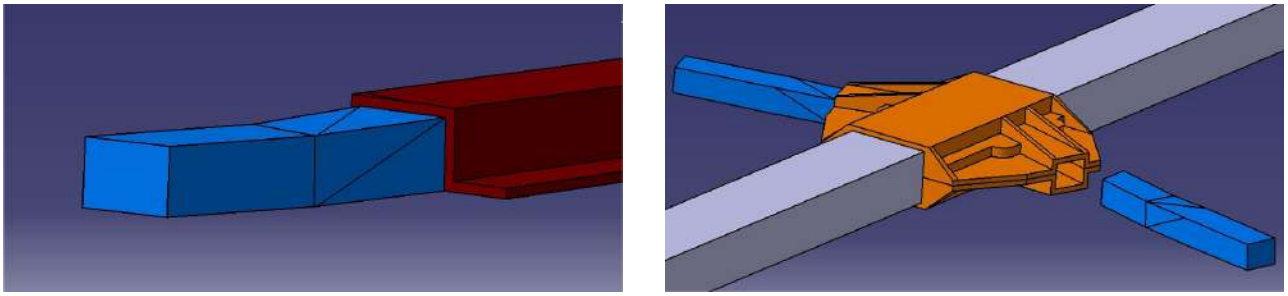

(a) Insert Geometry

(b) Insert Assembly method

Figure 19: Insert Concept

It is important to note the adaptability of the final result. The fuselage beam should be seen as a rail along which the "Wing to Fuselage connection" could slide. Different holes could be drilled along the fuselage beam for the positioning allowing for a variety of functional configurations, serving as a framework for future investigations.

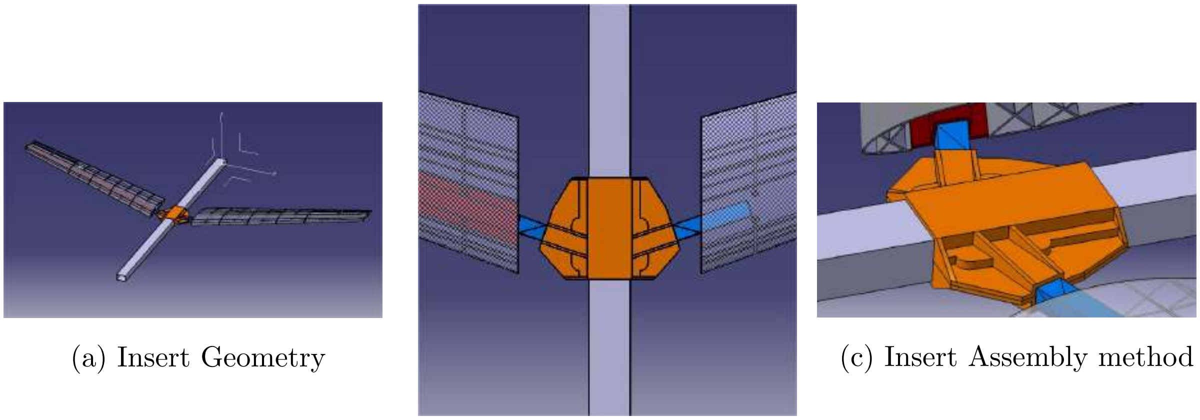

(a) Insert Geometry

(b) Insert Assembly method

(c) Insert Assembly method

Figure 20: Insert Concept

4.6 Tail To fuselage Connection

4.6.1 Initial Concept

Again there was the need to connect the tail geometry to what should be regarded as the main structural component, the fuselage beam. Following a similar approach as the one previously illustrated for the "Wings to Fuselage Connection", a clamping mechanism that would enclose the beam was initially conceived as base anchoring point for the rest of elements required (yellow part in Figure 21).

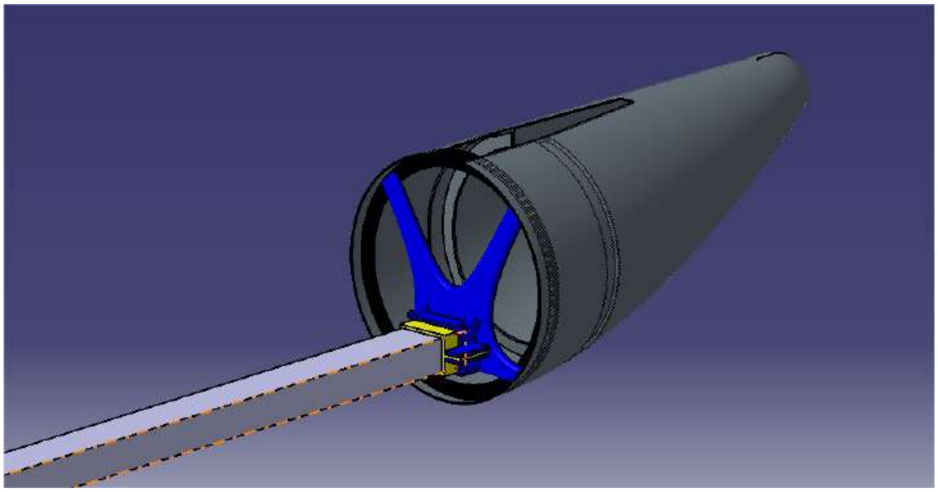

Figure 21: Framework for Tail Cone Assembling

The main concept behind this design was to connect the elements that would transmit forces directly to the fuselage beam, making the tail cone just a lid that would cover the structure. In consequence the tail cone no longer behaved as a structural element and the anchoring points on the cone could be made slimmer. Due to the closing nature of the cone, a slit would have to be cut in order to allow through the structure that would hold the tail in place.

From previous use it had served, the tail cone's bolting holes had been ripped and were no longer functional. Consequently, it was vital to grant the structural integrity of the cone. This was achieved by designing an aluminium ring that would act as as a circular rib. This rib served the double purpose of stiffening the tail cone while at the same time providing new functional geometry for bolt-holes.

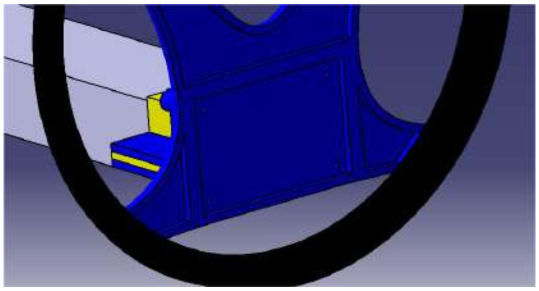

Figure 22: CNC Machining to increase Structural rigidity

Moreover, a radial rim like part was designed to link both the beam clamp and the machined ring adhered to the tail cone. The planar morphology of this link implied that it would be sensitive to bending. So as to reduce these weaknesses, the milling was extended at certain regions, taking the moments of inertia axes out of the plane and in consequence making it less compliant.

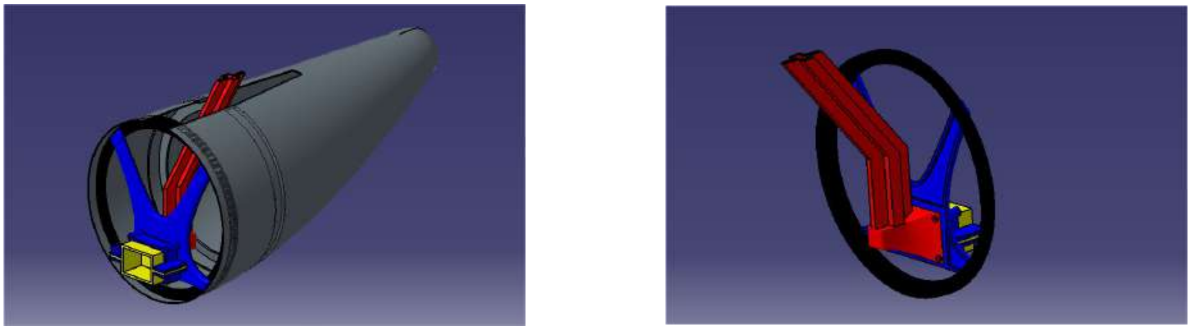

(a)

(b)

Figure 23: Tail Assembly Structural Elements

Following the mentioned machining, a centering square was designed to allocate the hammer like pillar (square in Figure 22). This pillar (red part in Figure 23a and Figure 23b)would be split in half to grant access to the interior where a cavity would be milled to match the vertical tail spar's geometry. Referring once again to Figure 23b, it may appreciated how the mast initially nucleates vertically from the hammer-head, and then turns to become parallel to the vertical tail spar, adequately positioning the whole tail geometry.

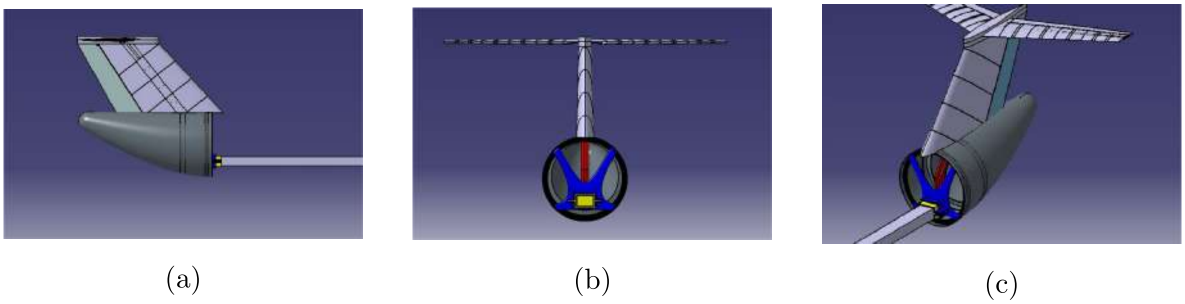
(a) (b) (c)

Figure 24: Initial Concept for Tail Assembly

4.6.2 Tail to Fuselage Connector Modification

During one of the meetings with the manufacturer, it became obvious that the manufacturing costs would be high, even though both the inner radial plate and the aluminium ring could have been manufactured from the same initial block.

Evaluating the alternatives, it was concluded that a previously available assembly, "Ordinata di Forza", could be adapted to meet the requirements. It was in turn more practical to work on the tail cone, which as previously mentioned was damaged, and restore its structural integrity by refurbishing.

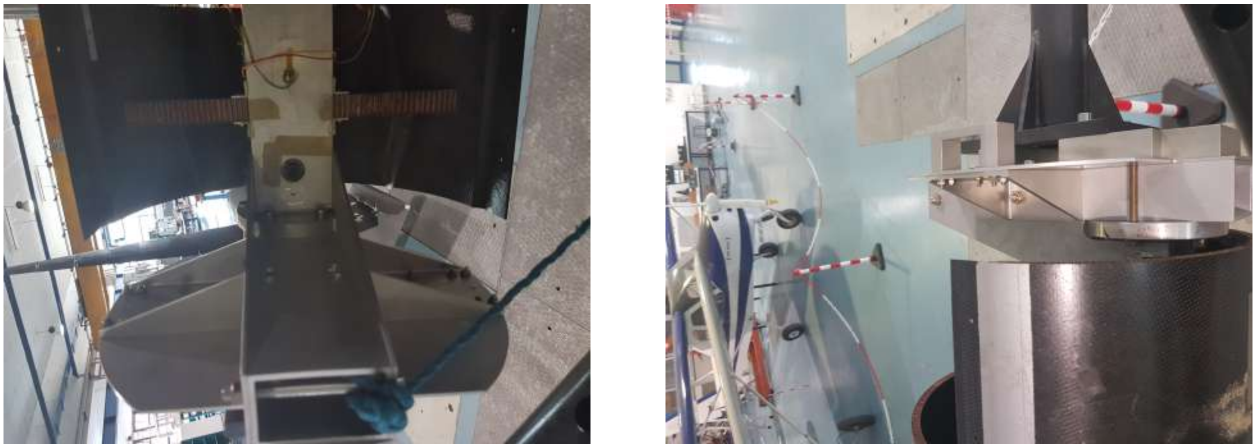
(a) (b)

Figure 25: Picture of the "Ordinata di Forza" mounted at DAER POLIMI Lab

This part was the one in charge of sustaining the wings in the previous negative sweep configuration, but the "U" shaped clamps would be no longer needed. In turn the Pillar shells as seen on Figure 23b could be adapted to work with the "Ordinata di Forza".

By extending the vertical tail spar's geometrical axis until it met the "Ordinata di Forza" plate and re-using the previously designed pillar, a new connection format was conceived. It resulted in a much shorter and simpler connection which in combination with the bolting capabilities of the "Ordinta" would result in a significantly stiffer solution.

As seen on Figure 26a the six holes located at the center could be used to attach the modified pillar. These six holes were previously used to anchor the part to a fix stand currently located at the DAER but will have no utility during testing as the model will be hung from cables and hence could be used to fix the pillar in position.

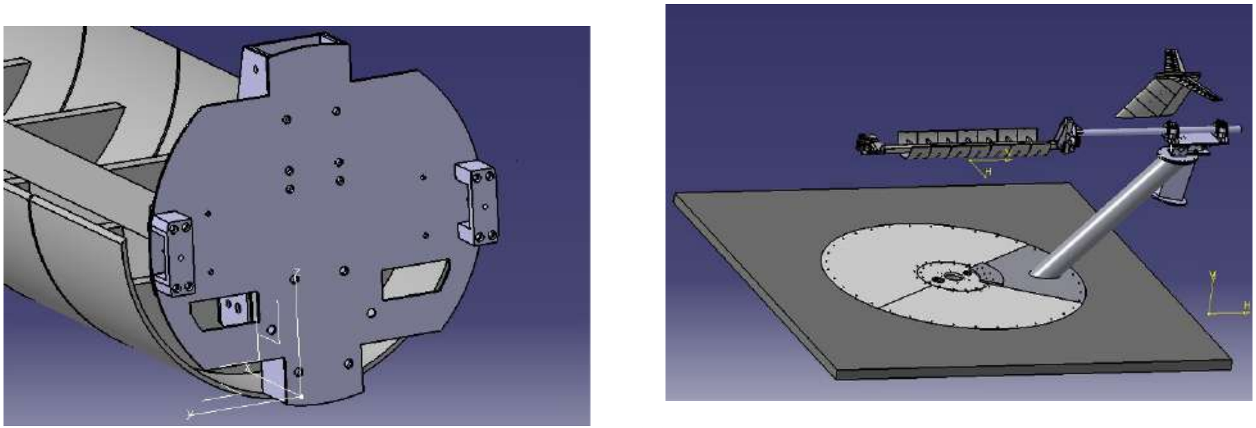

(a) Rear View of Ordinata di Forza

(b) CAD model of Mechanism to Control Pitch and Roll

Figure 26: Previous use of "Ordinata di Forza"

Consequently, due to the ease with which the pillar could be connected to the "Ordinata di Forza" the number of parts to design reduces from 5 to 2. Only the pillar was re-designed and had to be split in two so as to allow for the interior milling of the cavity that would hold the tail spar. Then the two halves would be joint to form a single mast, just as in the previous concept.

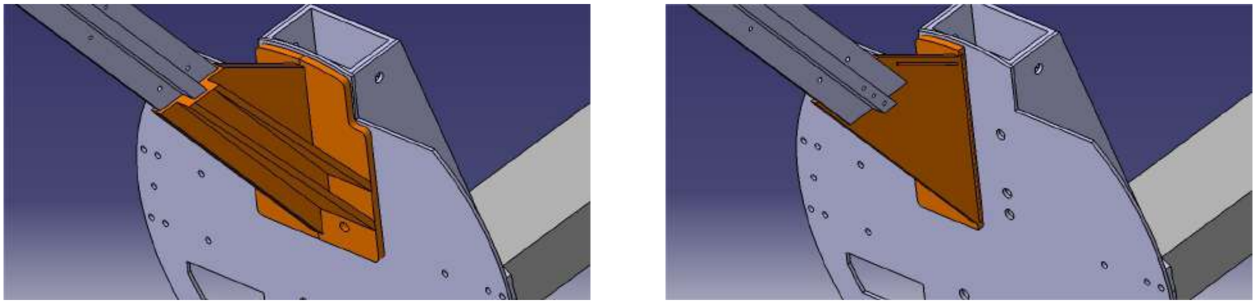

(a) Exterior Pillar Geometry

(b) Interior Cavity for Spar

Figure 27: Final "Tail to Fuselage" Connector

4.7 Horizontal Tail Trimmer

As any other flying plant, the scaled X-DIA had to have the ability to grant both equilibrium and some acceptable static margin. As the ailerons would be implemented in the AFS, it was decided to make trimming totally independent of the wings and take it to the tail plane. As in many other commercial aircraft, the horizontal stabilizer was made a trimming stabilizer.

Figure 28: Tail Configuration

The concept developed was one in which the hole horizontal tail plane could be pre-set at a given angle depending on the flight conditions. Due to the "T" shaped tail geometry it was obvious that some hinging mechanism about the leading edge of the assembly would allow to easily modify the deflection angle of both stabilizing surfaces simultaneously .

As the trimming did not have to be dynamic, an effective but rigid part was conceived. Using the previous beams and spars that structurally composed the tail structure, it was simple to produce a hinge capable of withstanding the aerodynamic loads. Following a similar argument to the one posed in the previous connection mechanism (Tail to Fuselage Connection) a mast in which to introduce the vertical tail spar was designed.

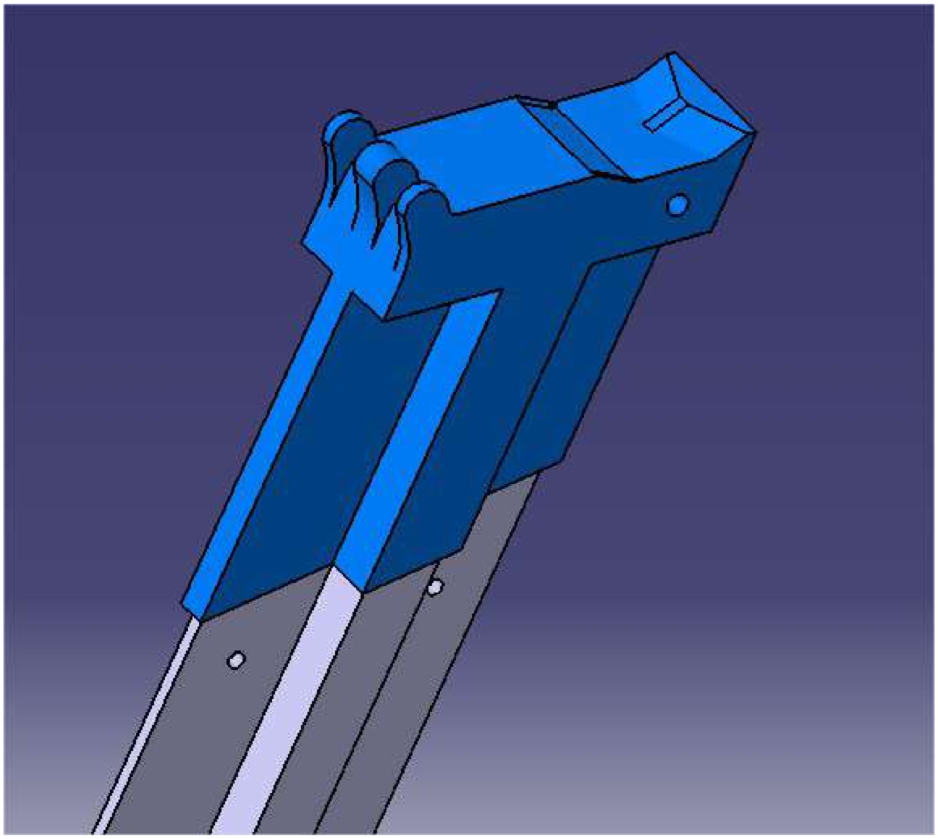

Figure 29: Hinge Mast Element

This design was extracted from a previous version, that had the same functionality but did not allow the trimming angle variation. The work done upon that design was to re-structure it so as to permit the aforementioned hinging.

Consequently the portion destined to fix the lateral spars that compose the horizontal tail sections was cut and extracted into a new ".part" that would follow the same concept but made independent of the mast (Green part in Figure 30a and Figure 30b).

Clearly from figure Figure 30a, it can be seen how the hinge will be milled to embed the horizontal tail spars. This provides a self centering interaction, that will in turn facilitate greatly the mounting process. The spars are then locked in position using a machined aluminium lid and fixed by the same bolts and holes as in its elder configuration (Figure 31).

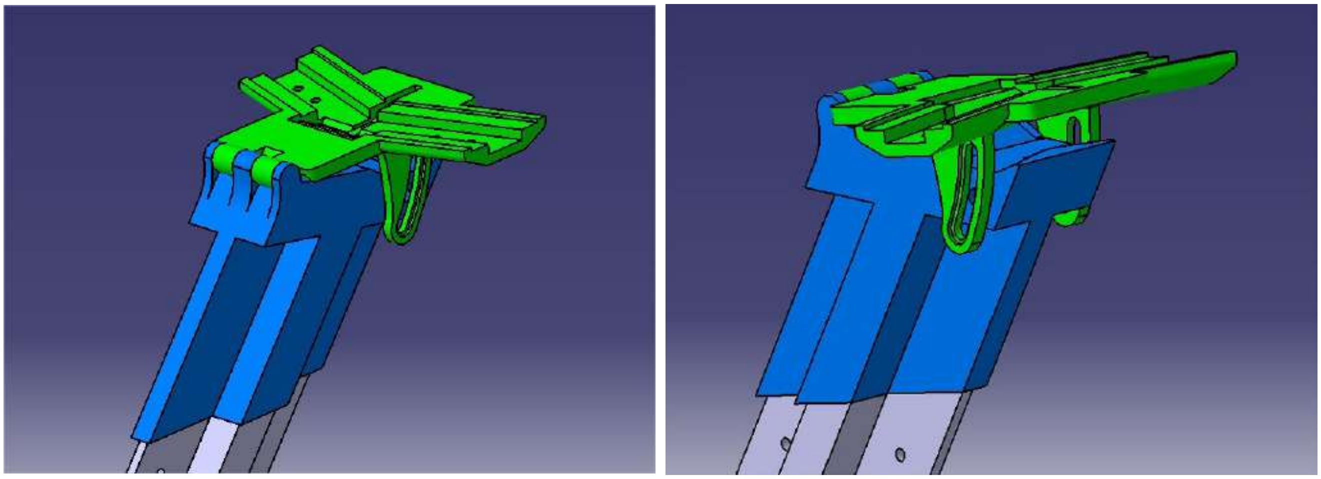

(a) (b)

Figure 30: Hinge Mounted on Mast

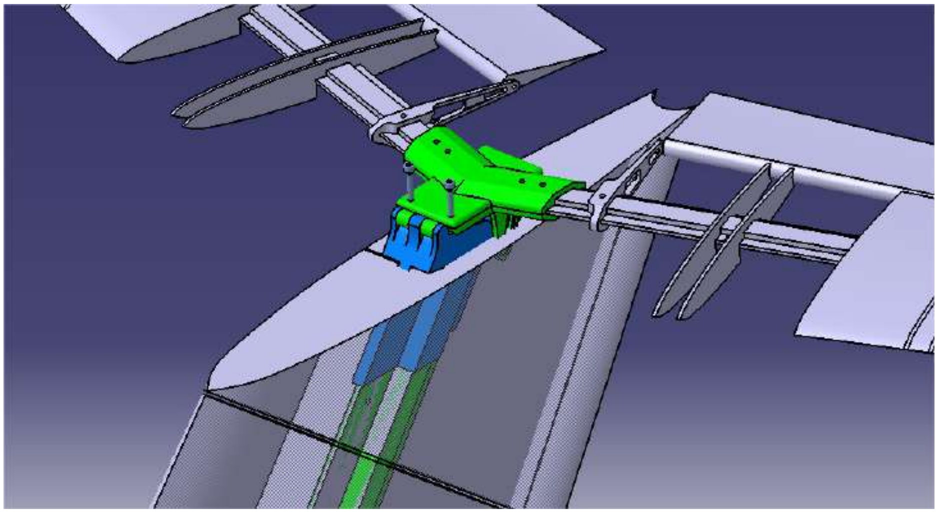

Figure 31: Mounted Hinge Assembly

So as to set a given angle it may be seen in both Figure 30b and Figure 31, a single screw has to be tightened. The hinging moment has its axis at the leading edge of the mast structure, and at the trailing edge where the two arch guides allow the rotation and are indented to match the screw heads. Basically the tail plane angle could be set at the desired incidence manually and the fixed in position by the screw.

4.8 Flutter Suppression Mechanism

Flutter, outside this investigation, is an undesired phenomenon. As quoted from Frazer, in [5] "flutter" means an oscillation which grows. Either if in explosive manner or in a moderate way, divergence could lead to structural compromise. If at some point the AFS failed to compensate the oscillations, some emergency reaction should be designed to avoid permanently damaging the experimental plant and to preserve the wind tunnel's integrity.

When dealing with possibly fast diverging attitude, the obvious decreasing of the wind tunnel operating speed is not sufficient. Despite the existence of some wind tunnel mechanisms such as the "q-stopper", which would rapidly shut down the wind tunnel by cutting the airflow, the speed control will inevitably have associated time delays which might be too slow to react in time to flutter or divergence and a much faster mechanism was needed.

According to [1] the placement of lumped masses at wing tip section will alter the flutter speed. From his work it can be seen that introducing a mass, specially towards the trailing edge, significantly lowers the flutter nucleation velocity, as already mentioned. This principle could be in turn used as a safety measure. If applied in the inverse manner, initially placing 2 masses offset from one another connected by a rod along which they could slide, and subsequent lumping of these two masses would rapidly vary the load distribution on the wing. In this case, the natural frequencies of the wing would immediately increase, causing the new configuration to have a higher $V_{flutter}$ while still flying at the same V_∞

The concept had to fulfil a number of requisites:

- Dimensional Constraints
- Functionality
- Response Immediateness
- Small Aerodynamic Perturbation

Inspiring on the Aermacchi MB-326 exhibited at POLIMI premises and more specifically on the pod like wing tip fuel tanks, it was possible to accomplish most of the demands.

As a starting point and to grant the required versatility, a wing lid was designed to close the last aerodynamic sector and to provide a homogeneous surface from which to develop the other components for the flutter suppression mechanism. Bearing in mind the possibilities that 3D printing yielded, the wing profile was extended up to a plane set parallel to wind direction. On figures Figure 32a and Figure 32c two centering plastic tabs were design to fit around the outgoing portion of the wing spar. Probably this plastic tabs will have to be complemented by a third tab as to provide the required robustness.

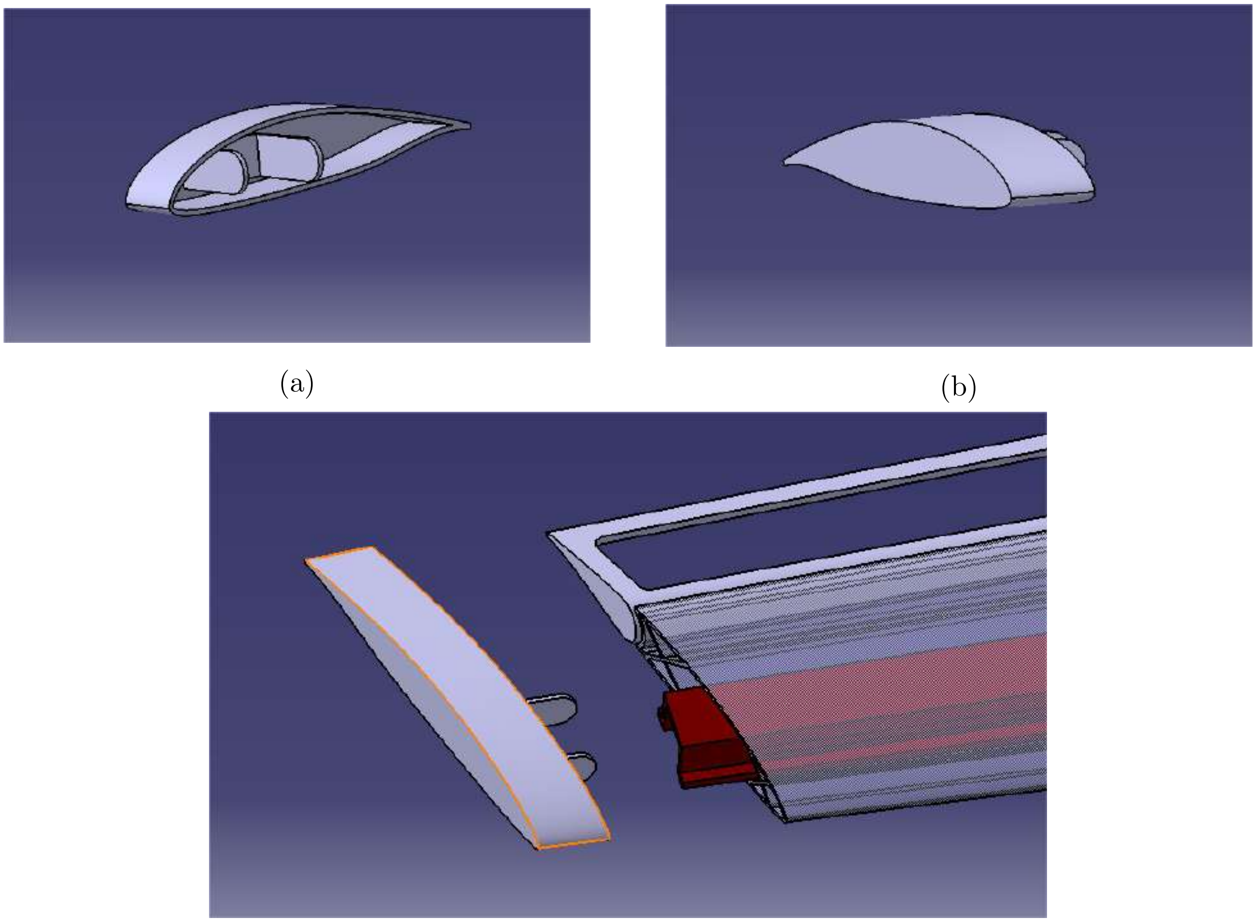

(a)

(b)

(c)

Figure 32: Wing Lid

The pod like structure was made independent of the wing lid because in that way, if future designs, with different geometries or dimensions were required, the pod would already have some anchoring mechanism available.

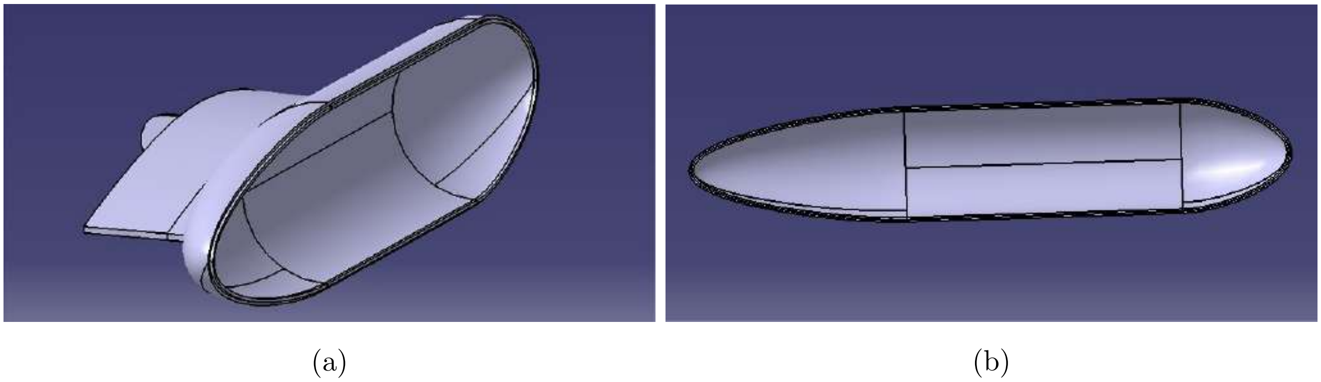

(a) (b)

Figure 33: Pod Lid Geometry

Formed by two cylindrical parts (Figure 33a and Figure 34a) the pod would enclose the inner flutter suppression mechanism (not developed yet). The idea was to have an exterior that would perturb as least as possible the air flow while granting sufficient space for the masses needed . After studying the plausible size of the masses, a 25mm inner radius was more than sufficient and the initial stage was set, but further development would have to be made.

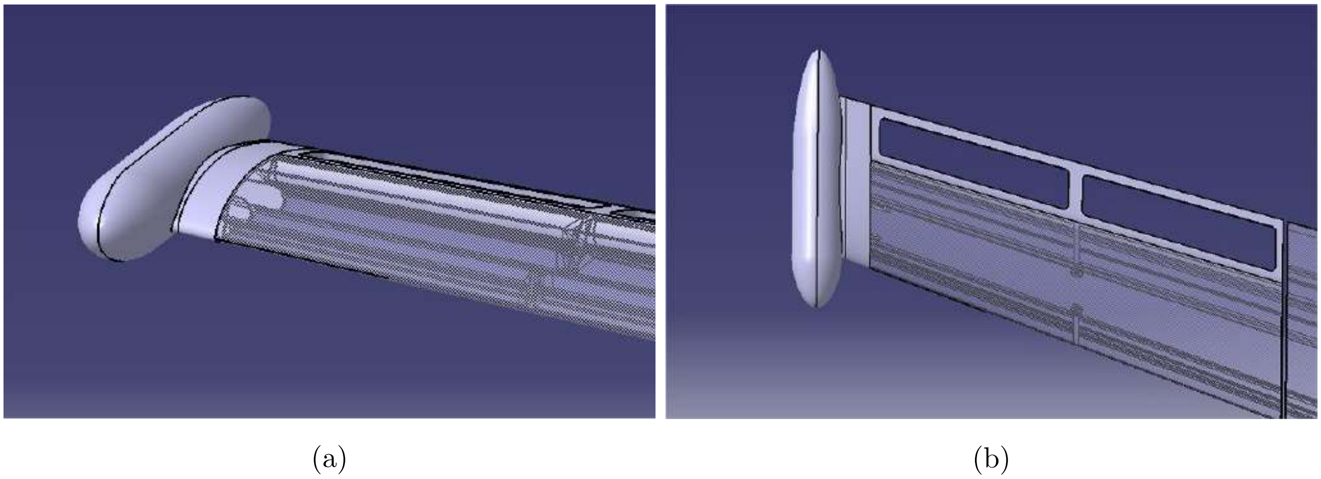

(a) (b)

Figure 34: Flutter Suppression Mechanism Pod

5 Modal Analysis of Designed Assemblies

5.1 Introduction

Up to this point the work had been focused on the initial steps of design. The aeroelastic nature of the model inevitably lead to the analysis of the modal modes of the different connection elements.

Structurally the most demanded assembly will be the one connecting the fuselage beam and the wing spar. As previously mentioned the NeoCass model had already been composed, and accounts for the simplified geometry where these connections were not explicitly modelled. In turn there was the need to characterize the new designed components and update the structural parameters of the pertinent rigid elements, mathematically modelling the overall behaviour.

Modal analysis in FEMAP using MSC Nastran illustrates both the fundamental frequencies and the mode shapes associated to each one of them modes. The use of this procedure has become an industry standard to initially characterize and further understand the structure.

Any given perturbation will inevitably set the structure into motion. This induced vibration is in turn a combination of some or all resonant modes associated to a model. Typically it is the lower frequency modes the ones that contribute the most in terms of displacement amplitude, and flutter is no exception to this phenomenon. As a consequence in the preliminary and intermediate design stages these lower frequencies are the ones to focus most upon.

In order to study the effect of the several parts composing the assembly a progressive analysis was performed. This allowed to study the impact of each individual element and to either validate or propose enforcement measures to match the required working conditions.

The decomposition of the analysis was performed in the following manner:

- Spar: Ideal Behaviour
- Spar and Insert
- Full Assembly

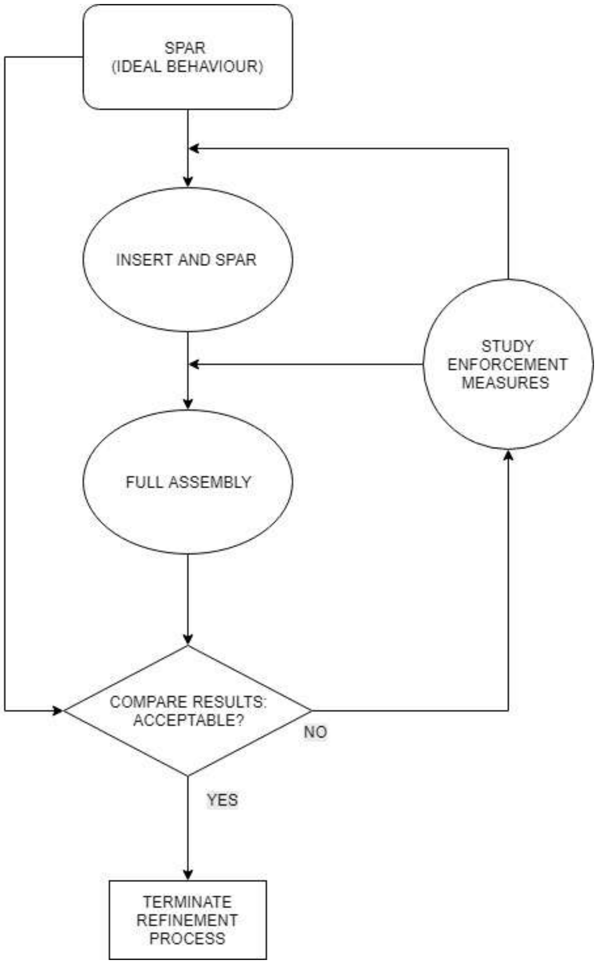

Figure 35: Analysis and Optimization Work flow

5.2 Ideal Behaviour

As a starting point, it was necessary to understand the wing spar. This is the behaviour that the whole assembly should match and hence the results against which any other analysis should be compared. The morphology of the wing spar allowed to use plate elements instead of using the whole solid as a model. The plate representation was defined using the mid-plane of the spar and then characterizing it with a uniform thickness of $3.6mm$. At this stage the exterior holes for the bolts had not been modelled yet but the FEA software allowed to model them despite not being physically present. The bolting axes are defined by the two sets of dots illustrated on Figure 36.

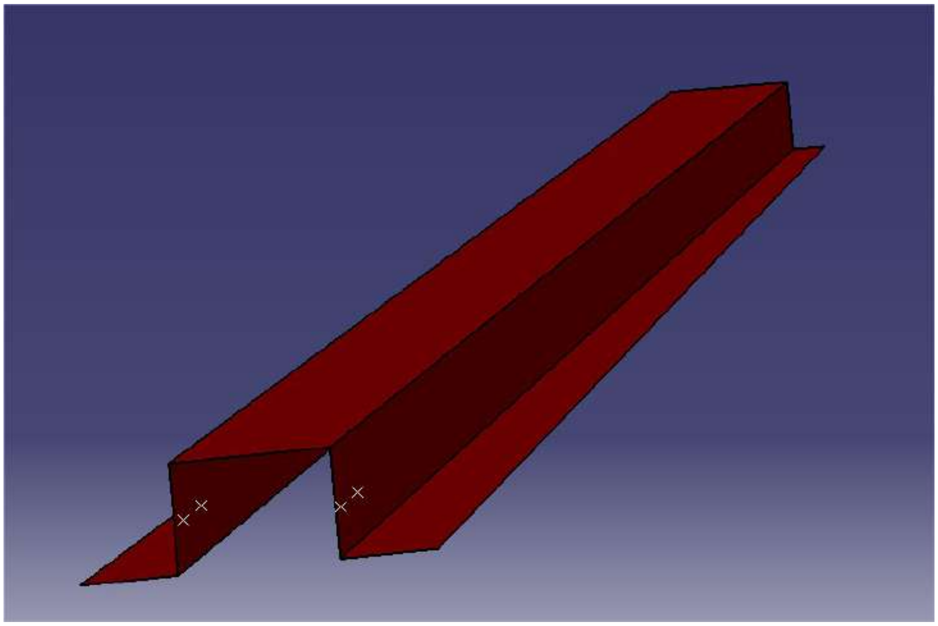

Figure 36: Spar Modelled by Plates

5.2.1 Finite Element Analysis Set-up

The spar was imported to FEMAP after a conversion from ".CATpart" to ".stp" format. FEMAP included one of the default libraries Aluminium 2011 T3 which as previously mentioned is easily machinable and hence ideal for these components. The only inconvenience was that CATIAV5 would associate a density of 2700 kg/m^3 to the parts while the real weight of the components would in fact be higher due to the real 2823 kg/m^3 density .

To study the modal behaviour, the wing spar was fixed in a similar way as the ideally, infinitely rigid assembly, would. The aforementioned points on Figure 36 were grounded, constraining all of freedom.

The spar plate geometry was meshed using NASTRAN's QUAD elements, generating an acceptable mesh thanks to the regular geometry of the spar. In order to model the bolting interaction, RBE2 elements were used. In this case the independent (master) element was the node to be grounded while the adjacent nodes were set as dependent and in consequence should not move due to the rigid nature of the RBE2 element.

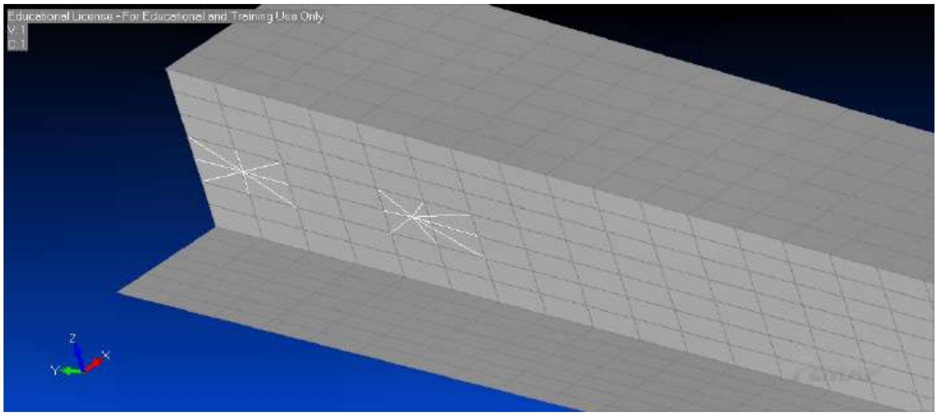

Figure 37: Bolt Simulation by means of RBE2 elements

Once the model was set it was now time to analyse and carefully study the results. The study was performed using NX NASTRAN as analysis program to solve the eigenvalues. This simulation was set to compute the first ten modes or modes up to $100Hz$.

5.2.2 Results:

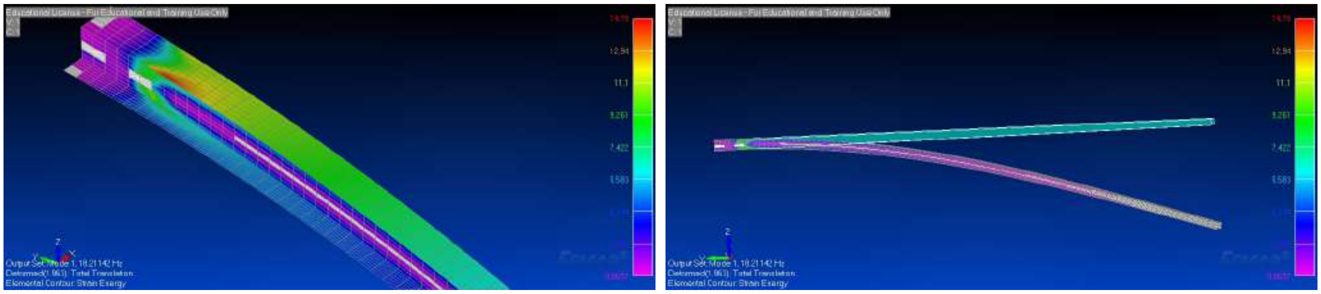

(a) Mode 1 (b) Mode 1

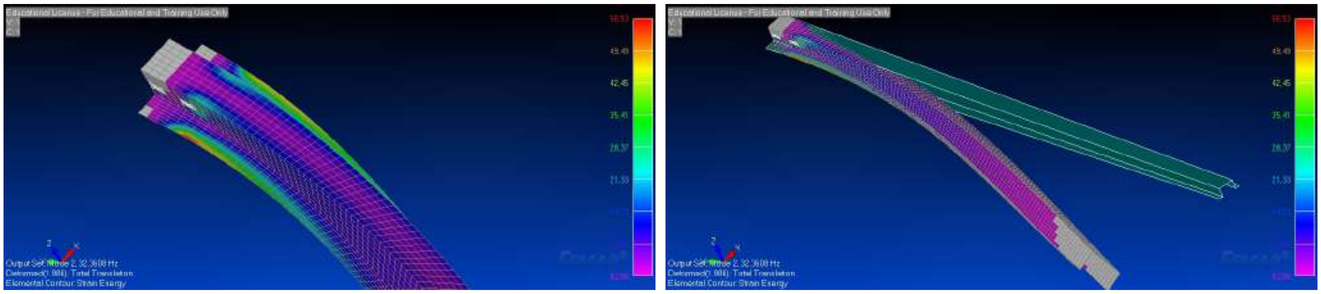

(c) Mode 2 (d) Mode 2

Figure 38: Spar Modes in Strain Contour

Table 4: Spar's Natural Frequencies

MODE	Frequency (Hz)
Mode 1	18.21
Mode 2	32.35

The first mode, the one associated with the greatest amplitudes is the main bending mode of the spar, while the second eigenvalue and associated eigenvector represents the bending torsional behaviour of the element in the wing plane, subsequent simulations will serve to understand the effect of the other components on the natural frequencies. The objective is to obtain obtain a connector assembly that will deviate at least as possible from the ideal behaviour frequencies in Table 4.

Obviously exact matching of eigenvalues will be impossible (it implies infinite stiffness of the connector) but evaluating the results will help optimize the structure so as to mirror as much as possible the wing spar which will in turn simplify the task of introducing the obtained information into the general X-DIA NASTRAN model (Figure 5).

5.3 Effect of the Insert on Wing Modes

5.3.1 FEA SETUP

At this stage, for simplicity, the model remained without the bolting holes and the connections would be modelled once again by RBE2 and RBE3 elements. A solid property was defined for the insert geometry, and it was meshed using tetrahedral elements that granted an acceptable mesh both in terms of Jacobian and number of elements.

Table 5: Insert Mesh Quality

Quality Check	Number Failed	Worst Value
Jacobian (> 0.6)	5	0.705
Tet Collapse (> 100)	0	9.093

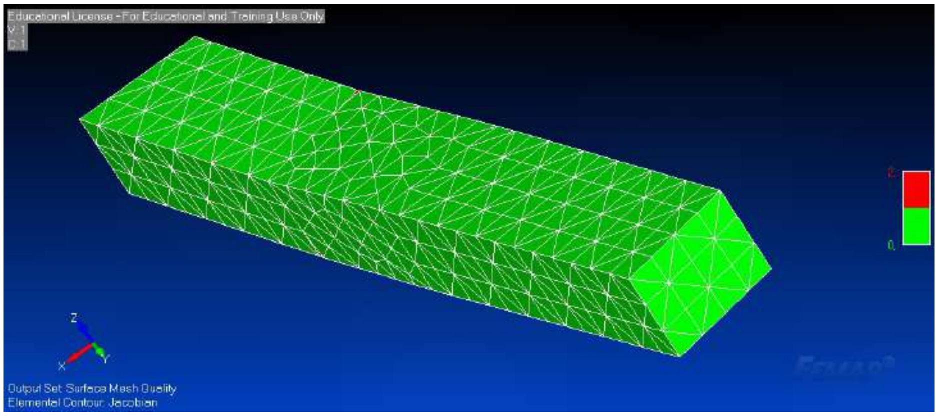

Figure 39: Insert Mesh Quality Check

NASTRAN's rigid elements were cascaded to define the rigid link (bolting) between the spar and the insert. First, to simulate the non-nodal effect of the virtual bolt-head on the spar's surface, a set of adjacent nodes were connected in spider manner to a central node representing the bolt axis as seen on Figure 36. This was done by means of a RBE3 element which computes the displacement of the central node by averaging the displacements (excluding rotations) of the elements on the spar surface. Moving inwards towards the insert, the bolt axis counterpart on the insert was rigidly connected as dependant node to the bolt axis node on the spar's surface by means of a RBE2 (6DOF related). Finally this node had to be connected to the nodes on the insert that would suffer the action of the bolt as seen on Figure 40b.

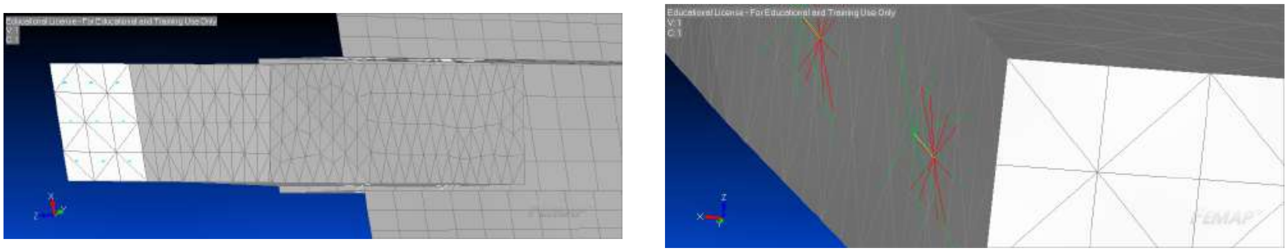

(a) General Overview of Bolting Simulation

(b) Cascading Rigid Elements

Figure 40: Insert and Spar FEA Set-up

In Addition, it was necessary to model the interaction between the inner surfaces of the omega sectioned spar and the top outer ones of the insert. This was done by defining a linear contact region between the mentioned surfaces illustrated on Figure 41.

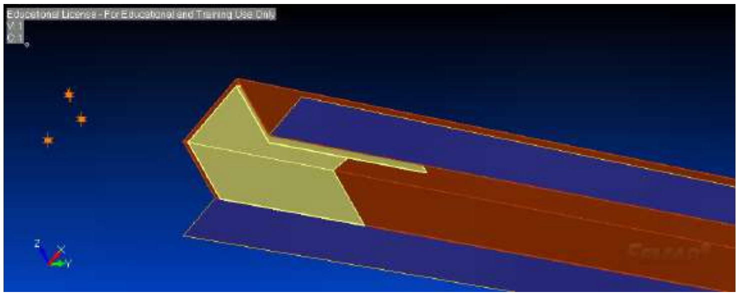

Figure 41: Linear Contact Regions Seen from below the Wing Spar

To complete the model, the boundary conditions were applied on the flat surface that would be in contact with the interior of the shell clamp Figure 42. Essentially this decision was taken in order to appreciate the full effect of the insert geometry on the natural frequencies and understand the intrinsic compliance of the insert.

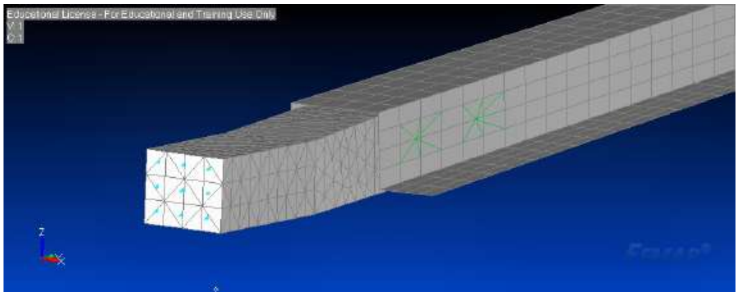

Figure 42: Constraint Approach

5.3.2 Results

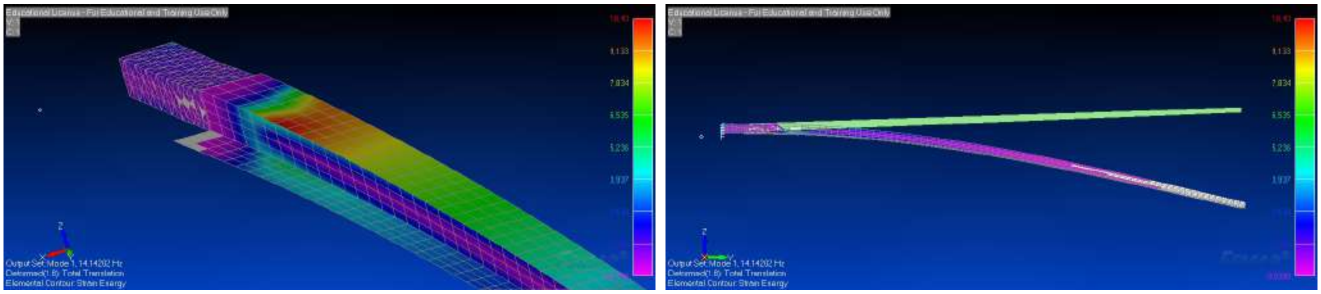

(a) Mode 1

(b) Mode 1

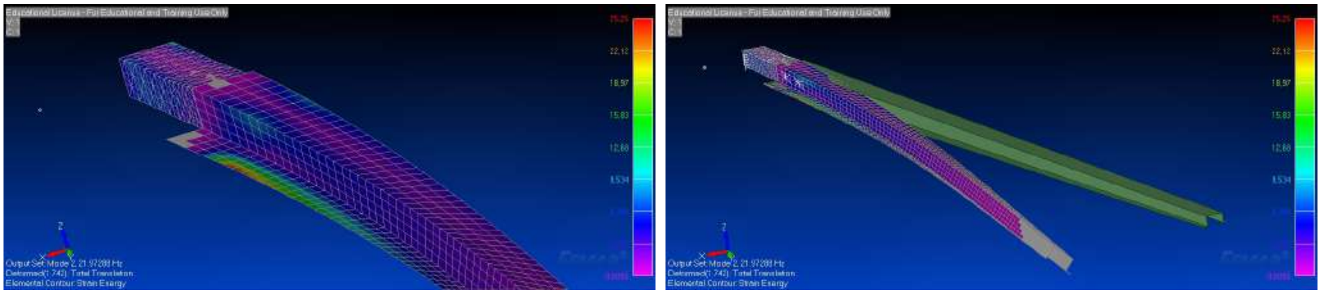

(c) Mode 2

(d) Mode 2

Figure 43: Spar and Insert Modes in Strain Contour

Table 6: Spar and Insert Natural Frequencies

MODE	Frequency (Hz)
Mode 1	14.14
Mode 2	21.97

At a first glance, the strain energy contours correlated between the ideal case and the "spar and insert". This meant that the insert was not varying significantly the eigenvector associated to each eigenvalue. Despite being similar for both cases (same contour morphology and position of maximum and minimum strain energy on the spar), the maximum value on with the insert was significantly lower (14.778 vs 10.432 for the first mode). When we look at the second vibrational mode, the difference is even more significant, as it dropped by over 50% (56.536 vs 25.264).

We could relate this lower strain energy to an increased compliance, and this hypothesis goes hand in hand with the natural frequencies obtained. Every mode is affected by the introduction of the insert and the modes tend to lower frequencies.

The way in which the simulation was set-up, had effectively elongated the wing spar, this longer characteristic length would account for the resultant lower natural frequencies.

$$[F] = [K][x]$$

if we invert the stiffness matrix [K] we obtain the flexibility matrix [C] which will better represent the impact of the overall increase in length.

$$[C] = [K]^{-1}$$

$$[C_{i,j}] = \begin{bmatrix} \frac{l^3}{3EI} & \frac{l^2}{2EI} \\ \frac{l^2}{2EI} & \frac{l^3}{3EI} \end{bmatrix}$$

This flexibility matrix is the one associated to a cantilever beam with one of it's ends fixed to ground and with 2 degrees of freedom.

From this matrix it can be seen how, the flexibility is proportional to the length cubed, so a slight increase in length would make the structure as a whole much more compliant.

Once all this said, the reader should bear in mind that this simulation was not explicitly representative of the overall assembly behaviour and that it was more important to ensure that no new modes were introduced by the insert and that the eigenvectors were as representative as possible of the eigenvectors of the spar alone, which they were as seen on Figure 43.

5.4 Full Assembly Vibrational Modes

5.4.1 FEA Set-up

Following up from the previously described model, the full assembly configuration required the introduction of new interactions between parts.

The first step, was to mesh the shell clamps. Following the same approach as before, coherent meshes for both solids were obtained while keeping the number of elements low so as to not exceed the FEMAPS's educational license restrictions and to reduce the computational load.

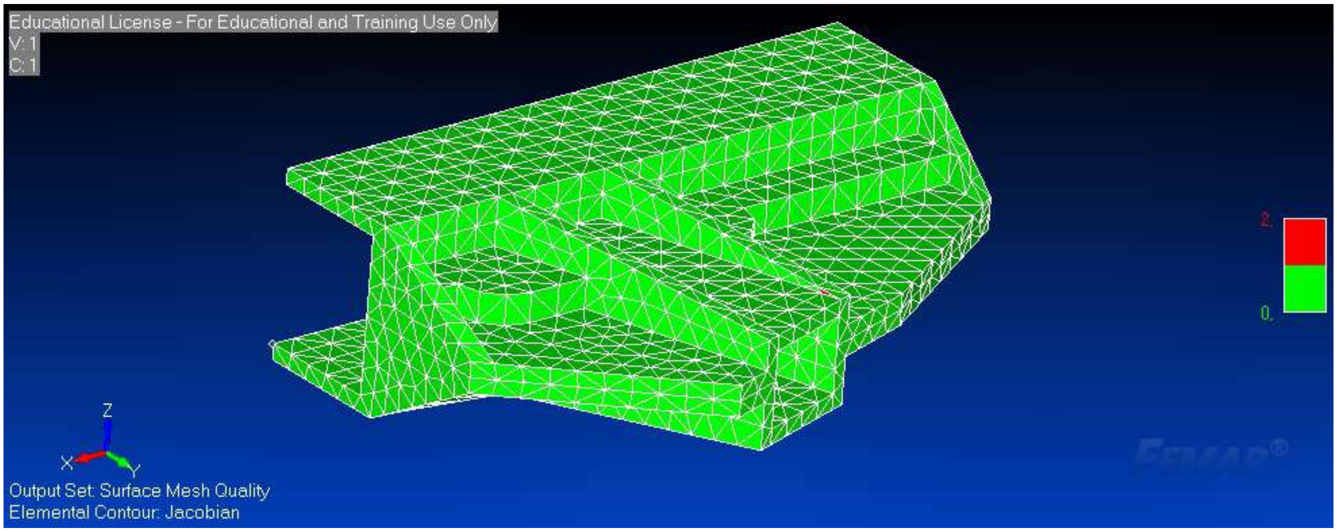

Figure 44: Quality Check of Shell Mesh

Table 7: Mesh Quality Clamps

Quality Check	Number Failed	Worst Value
Jacobian (> 0.6)	8	0.749
Tet Collapse (> 100)	0	11.452

For simplicity, the clamps were considered to work ideally, by this it is meant that compatibility was ensured between the two flat surfaces in contact. If the previous held, it was possible to weld the two shells together in addition to the insert portion that would be clamped by the two solids. This welding region is characterized by the grey surfaces depicted on Figure 45. Combined with the already existing contact regions between spar and insert that were defined in Section 5.3.1 the "self interactions" of the system had been modelled.

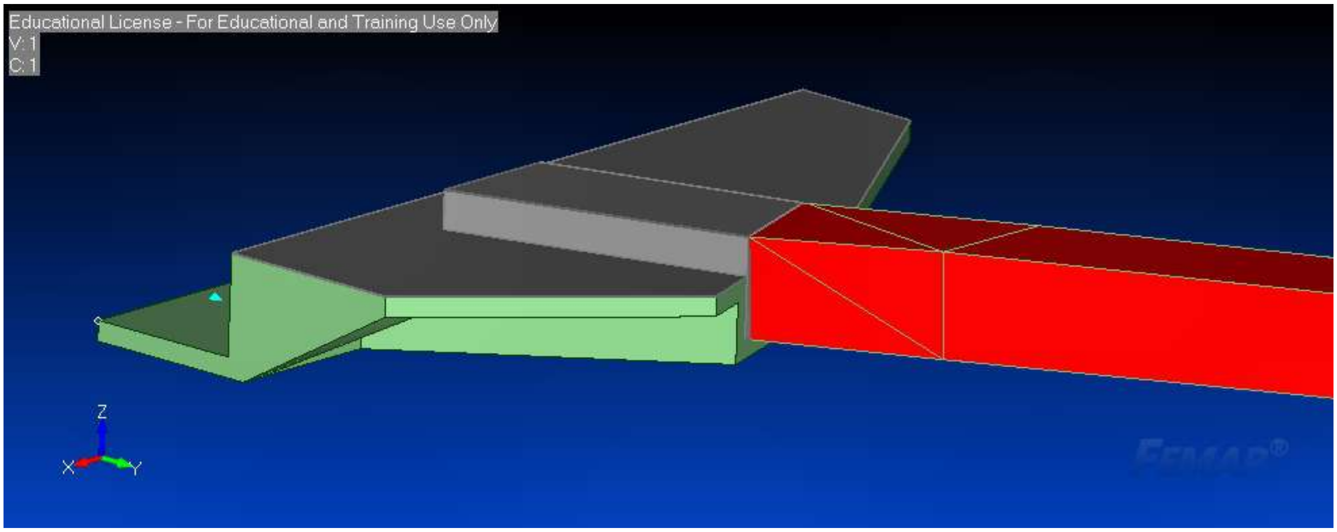

Figure 45: Welding Regions

Lastly, it was a matter of constraining the assembly and this was done by fixing to ground the surfaces that would be in contact with the fuselage beam, basically assuming the fuselage beam to be infinitely stiff.

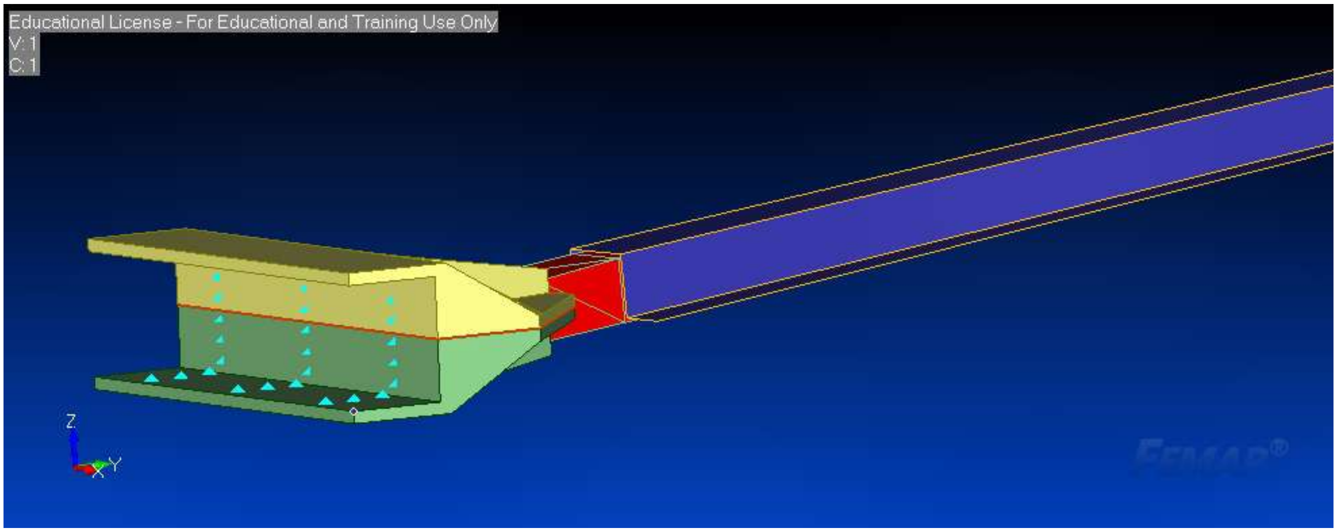

Figure 46: Constrained surfaces

5.4.2 Results

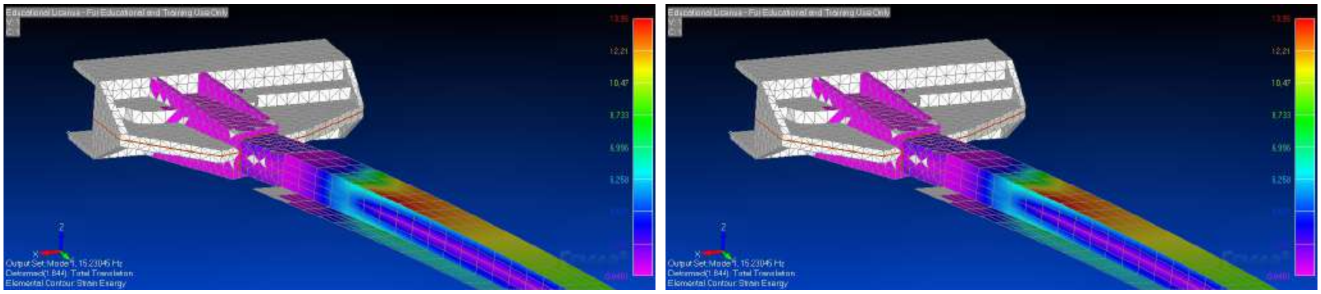

(a) Mode 1

(b) Mode 1

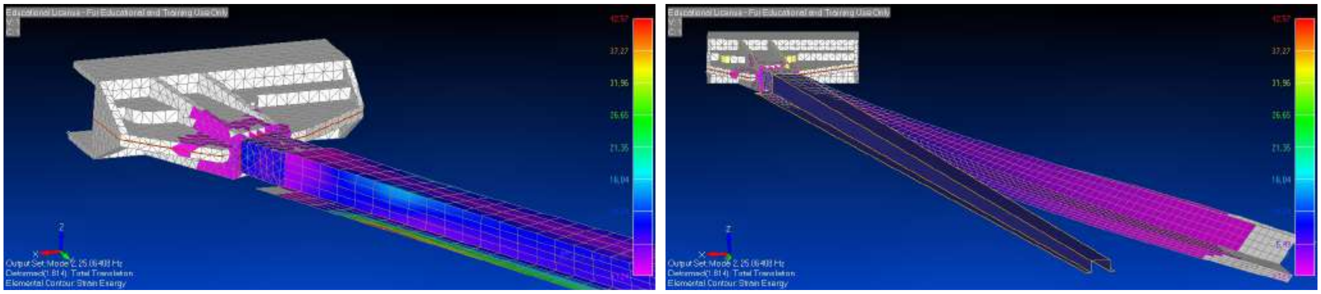

(c) Mode 2

(d) Mode 2

Figure 47: Full Assembly Modes in Strain Contour

Table 8: Full Assembly Natural Frequencies

MODE	Frequency (Hz)
Mode 1	15.23
Mode 2	25.06

Naturally, this time the mode frequencies increased to be closer to those of the ideal values. This favourable progression makes sense due to the fact that the whole system is more restrictive. In the previous case where only the insert and the spar were studied, the insert was basically behaving as a cantilever beam. Contrarily, in the current set-up the shells are firmly fixed to ground, and the geometry clamps a large portion of the previously unrestricted lateral surfaces of the insert.

Despite still being far away from the objectives, it should be noted how once again the vibrational modes were still representative of the ideal ones. This meant that the proposed design did not induce new natural modes in the structure and in consequence could be regarded as a valid candidate if further enforcement techniques could be applied to take the bandwidth towards that of the spar.

5.5 Wing to Fuselage Assembly Modifications

Following from previous work done, it was proposed to use a similar enforcing technique as the one developed for the so called "Ordinata di Forza". The approach was identical to the one highlighted in Figure 48, but there where some geometrical difficulties to solve beforehand.

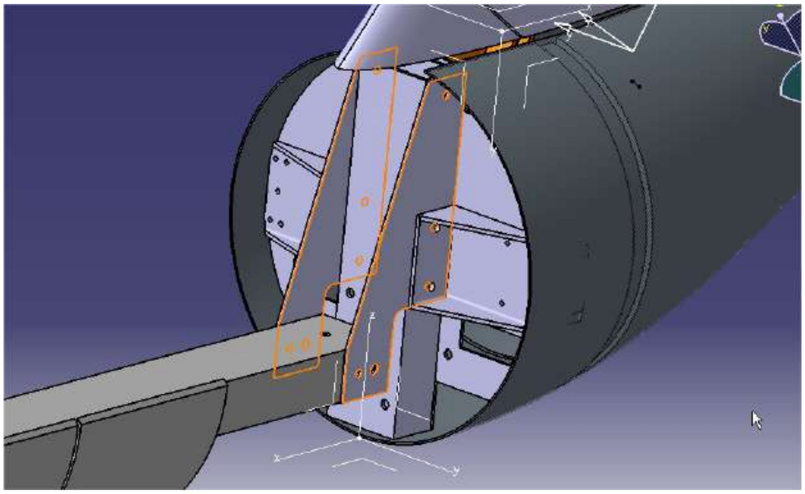

Figure 48: "Ordinata di Forza" enforcement method

The positioning of the spar within the wing sectors introduced the rotations of all three angles; the sweep angle, the dihedral and the mounting angle. These rotations in turn implied that the insert had intrinsic torsion and hence there were no aligned planes along which to introduce the enforcing plates and it was also plausible that the angle variation between the section destined to fit in the clamps and the section that would fit in the spar (which may be seen in Figure 49a), was increasing the compliance of the first bending mode.

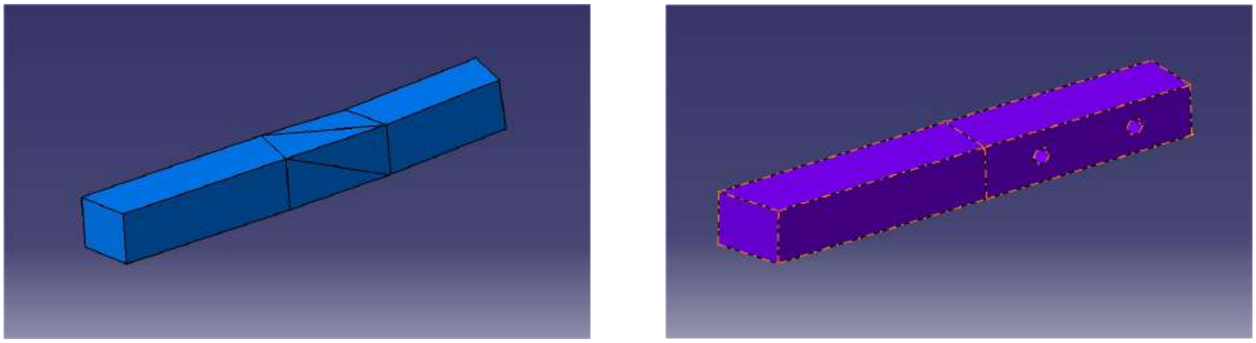

(a) Original Insert Geometry

(b) New Insert Geometry

Figure 49: Redesigned Insert Comparison

In consequence it was convenient to re-position the spar within the aerodynamic sectors so that to remove the effect of the mounting angle allowing for a straight insert axis. These modifications lead to a much simpler insert morphology, but in consequence inevitably complicated the clamping structures, as the cavities destined to host the inserts were no longer flat.

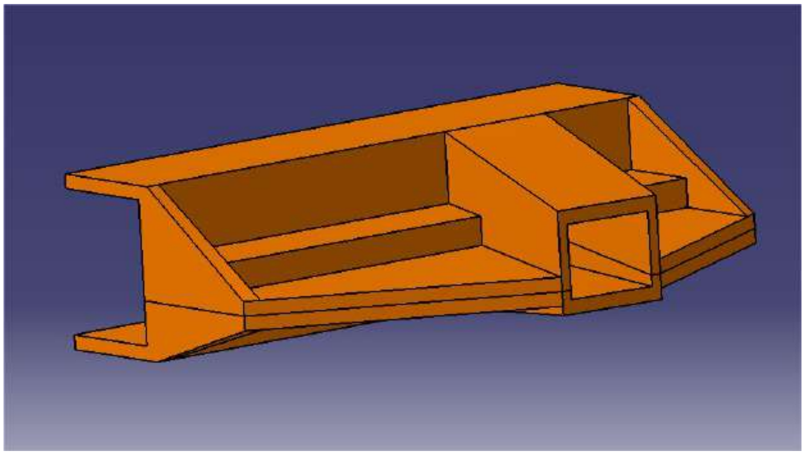

Figure 50: Split Modified Shells

With respect to the clamping shells some further modifications were introduced to facilitate the implementation of the enforcing plates. Firstly, the contact planes between shells were lowered down to allow extra space for the bolting of the insert which was fairly limited beforehand and could pose some manufacturing problems. To continue the vertical stiffener was completely filled and made trapezoidal to follow the same tapper as that of the wing spar. As a consequence the enforcing plates could be designed to be flat, gaining in simplicity and stiffness (Figure 51).

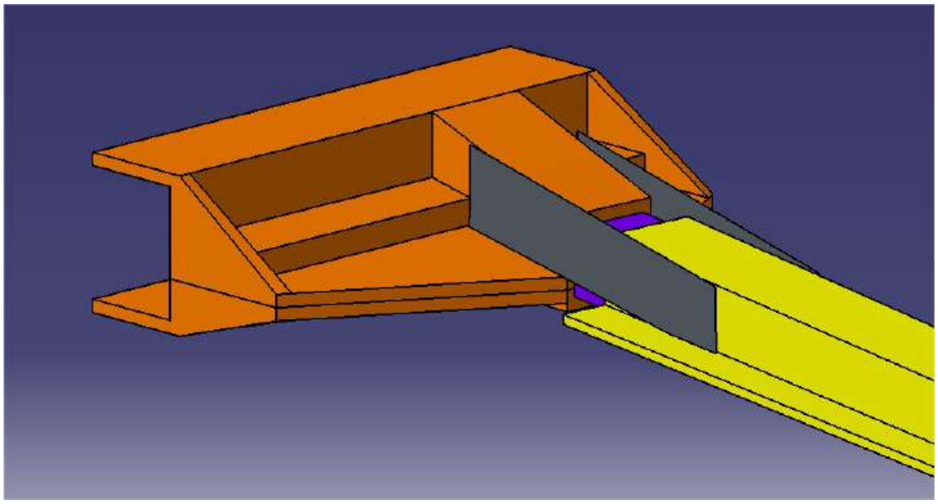

Figure 51: Full Assembly Configuration After Modification

5.6 Effect of Insert on Wing Modes After Modification

Once again it was important to study the full effect caused by the geometry and hence the same approach of gradually introducing elements so as to judge their individual impact, was followed.

In this case the pinning position to fix the spar to the insert had been decided and hence the holes had already been modelled in the updated CAD. The inclusion of the holes in the simulation should not be regarded as a problem. If the assembly managed to work in the desired frequency range with the holes, which inevitably weaken the insert, it would mean that it would perform even better without them. In essence, including the holes meant analysing the "worst case scenario," and acceptable performance under these conditions would allow the validation.

5.6.1 Results

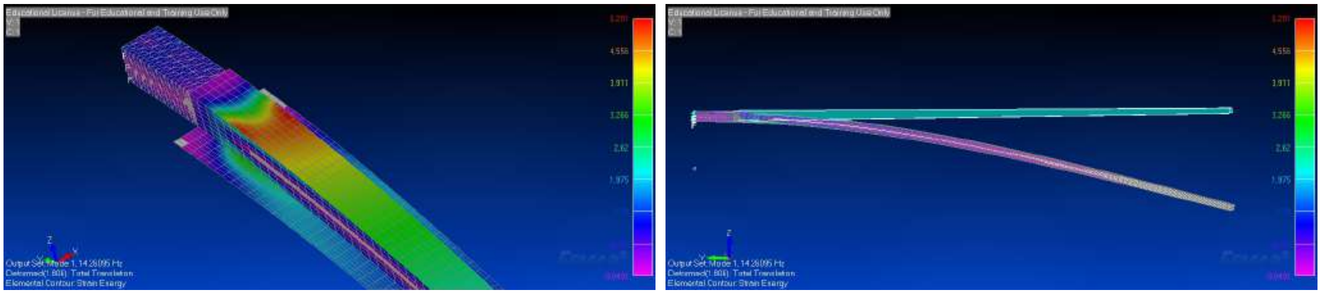

(a) Mode 1 (b) Mode 1

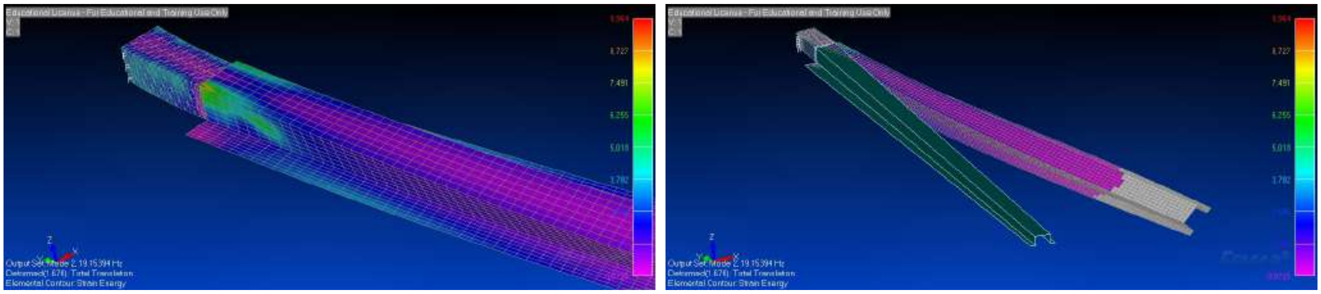

(c) Mode 2 (d) Mode 2

Figure 52: Spar and Modified Insert Modes in Strain Contour

Table 9: Straight Insert and Spar Natural Frequencies

MODE	Frequency (Hz)
Mode 1	14.26
Mode 2	19.15

After using the same approach to compose the FEA model, FEMAP's post-processing facilities allow us to study the effect of the geometrical modifications. Direct comparison between the two results yielded that in the case of the bending natural frequency (mode 1) there was a slight improvement towards the objective value of $18.21Hz$. This modest benefit should be associated to the straightening of the insert axis.

On the other hand, the torsional behaviour is further diminished, and not slimly. The new geometry becomes more compliant torsionally. Initially surprising as it may seem it should not be forgotten that the intrinsic twist of the original insert (Figure 49) could have made it stiffer in this bending-torsional mode.

5.7 Full Assembly Modes After Modification

5.7.1 Results

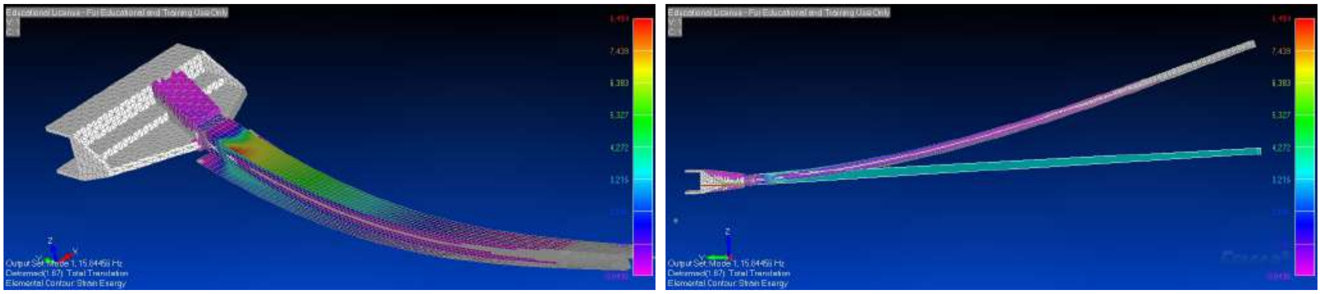

(a) Mode 1 (b) Mode 1

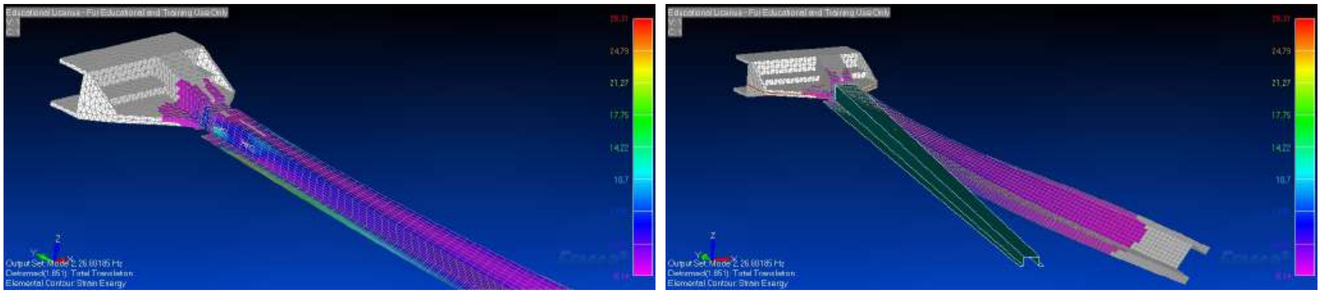

(c) Mode 2 (d) Mode 2

Figure 53: Full Modified Assembly Modes in Strain Contour

Table 10: Modified Full Assembly Natural Frequencies

MODE	Frequency (Hz)
Mode 1	15.84
Mode 2	26.60

As in the previous simulation the major encasement of the shell around the insert causes the frequencies to increase towards the goal. In this case both modes are benefited compared to the preceding example because the downgrading effect of removing the intrinsic torsion is now compensated by the stiffeners around the insert cavity.

5.8 Full Assembly enforced with Plate Elements

To sum up the progression, the two plates are included in the simulation. The plates were connected to the spar using RBE2 rigid elements using as reference the point set for the bolt axis. On the side of the wing to fuselage connection, the plates were fixed using a welding property for simplicity.

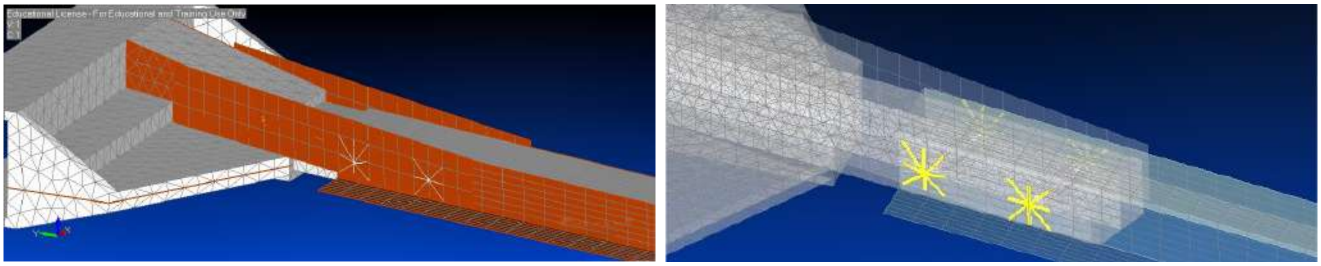

(a) Welding Region

(b) RBE2 rigid elements definition

Figure 54: Assembly with Plates FEA Set-up

5.8.1 Results

Progressively the frequencies become more coincident to those that were initially set as the "ideal behaviour". At this design stage the bending and bending torsional modes still differ by about 10% from the pre-set. This in turn triggered the debate as in what other methods could be used to stiffen the connection, as from all simulations it was clear that the insert was weakest element.

Table 11: Simple Plate Natural Frequencies

MODE	Frequency (Hz)
Mode 1	16.68
Mode 2	29.68

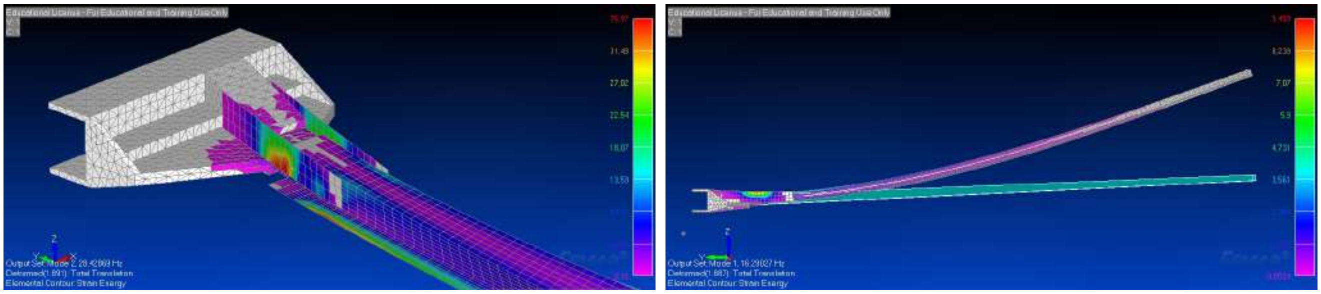

(a) Mode 1 (b) Mode 1

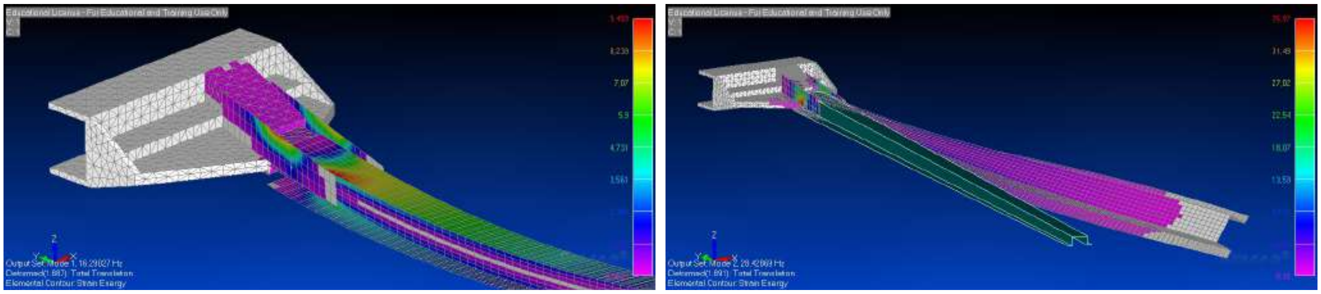

(c) Mode 2 (d) Mode 2

Figure 55: Modified Assembly with Plates Modes in Strain Contour

5.9 Steel Insert

An obvious step, at this stage was to study the impact of the material on the stiffness of the element. Despite using tempered aluminium alloy (2011 T3), hard enough for machining, its Young Modulus is still significantly lower (one order of magnitude), than that of 4330 steel.

The main drawback of this approach was the significantly higher density of the steel and how that would impact on the overall mass of the model, as the wing to fuselage connection was already the heaviest component.

Table 12: Comparison Aluminium 2011 T3 vs. Steel 4330

Material	Density (kg/m^3)	E (GPa)
Aluminium 2011 T3	2823,402	70,33
Steel 4330	7833,394	206,84

As seen on Figure 12 the density of the steel alloy is more than double that of the aluminium. In order to reduce the impact of the density in the overall model mass, the possibility of implementing a hollow steel insert was studied. In order to make it standard, 5mm thick walls were used.

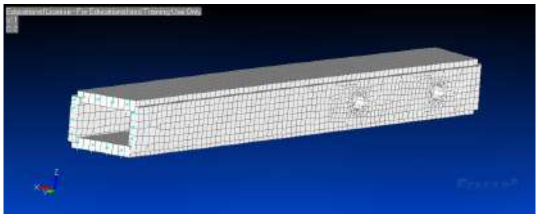

Figure 56: Hollow insert modelled by plate elements (thickness made visible in FEMAP)

5.9.1 Results

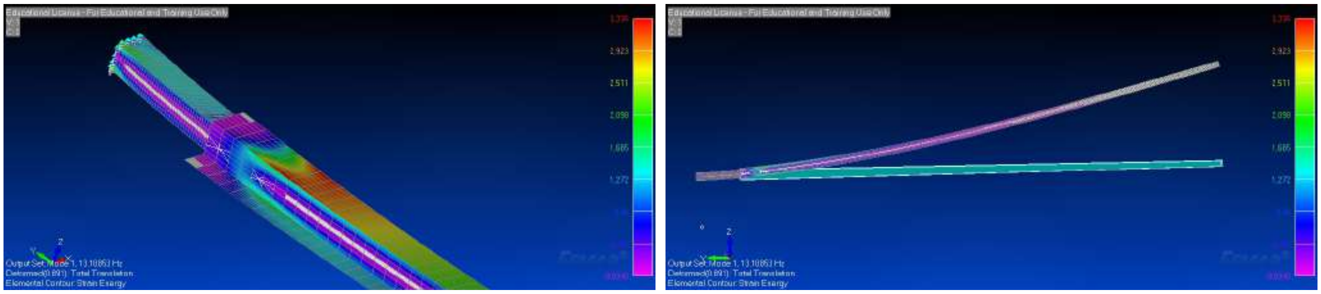

(a) Mode 1 (b) Mode 1

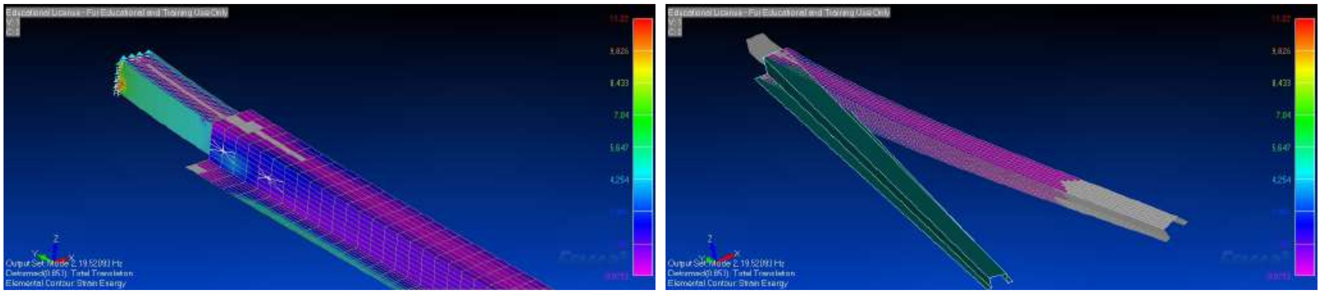

(c) Mode 2 (d) Mode 2

Figure 57: Steel Insert Modes In Strain Contour

MODE	Frequency (Hz)
Mode 1	13.11
Mode 2	19.52

In this case and the despite the higher Youngs Modulus of the steel, the significant material removal for the hollowing, caused the mechanical properties to be lower than those that were required. Comparing directly these results with the previous solid aluminium insert (14.26 Hz and 19.15 Hz), a slight benefit in torsional mode is appreciated while the bending mode decreases by over 1Hz.

Bearing in mind that the first mode (bending eigenvector) will be one with greatest presence in the flutter, then it is obvious that the use of a steel insert will have no positive impact on the overall performance of the assembly. This in consequence will lead to the discarding of this approach.

5.10 Effect of Elongated Plates

The clamp geometry allowed to increase slightly the enforcement plates and to add a new contact point. This was expected to positively contribute to the performance of the assembly, but its impact had to be studied in advance.

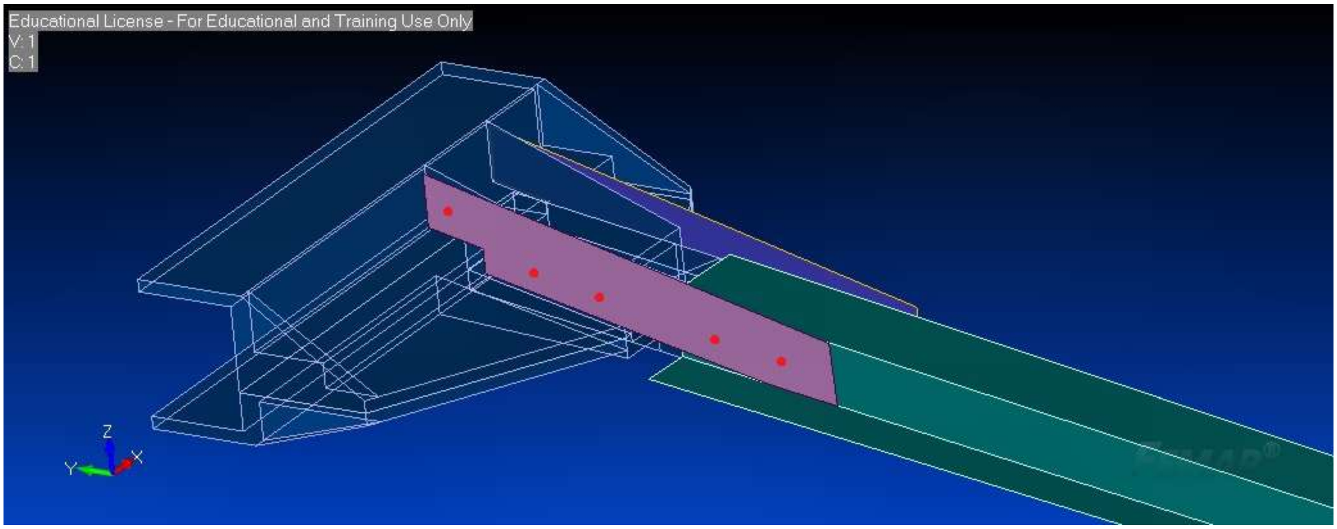

Figure 58: Extension of Enforcement Plates, Red Dots Representing Connection Points

5.10.1 Results

One again a similar approach to the rest of simulations was followed and the this time the impact was significant.

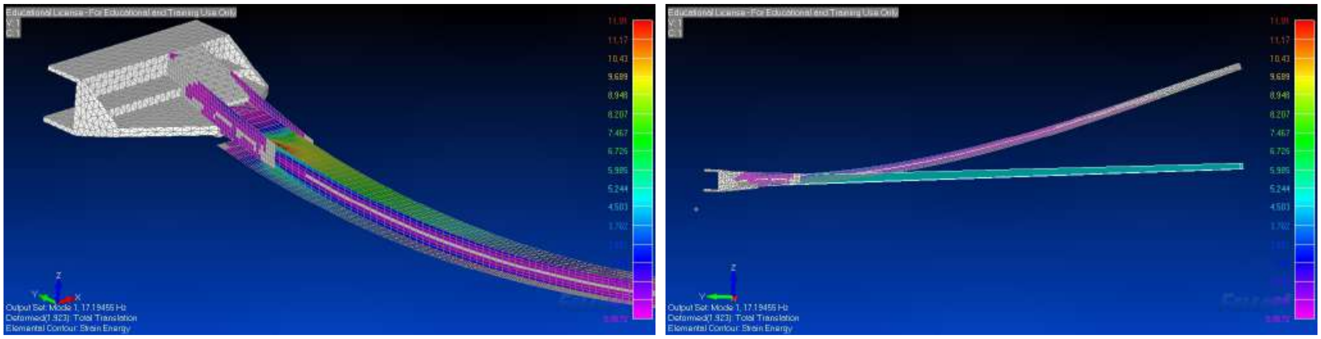

(a) Mode 1 (b) Mode 1

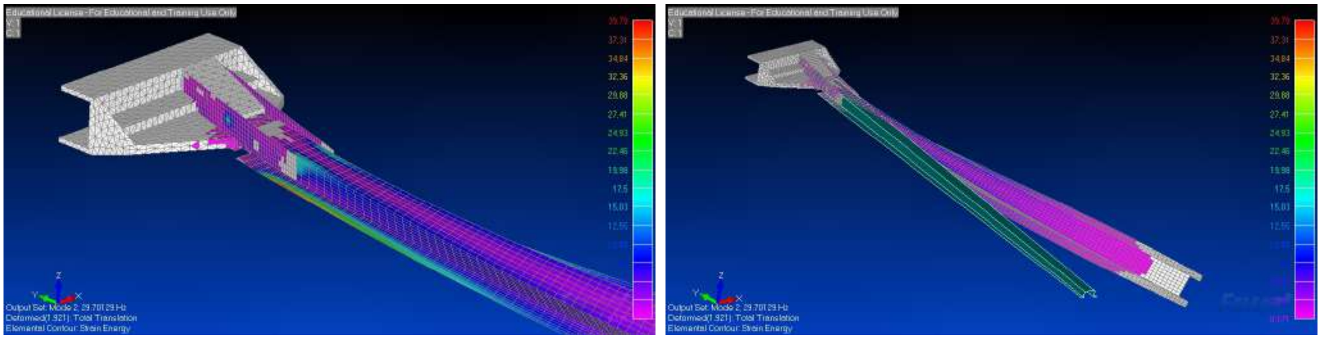

(c) Mode 2 (d) Mode 2

Figure 59: Analysis Results Assembly with Elongated Plates Modes in Strain Contour

Table 13: Modified Assembly With Elongated Plates Natural Frequencies

MODE	Frequency (Hz)
Mode 1	17.19
Mode 2	29.70

So now we finally have an assembly configuration capable or quite accurately matching the natural frequencies of the ideal spar. This analysis and optimization process has involved a number of simulations and the study of several techniques and the progress of this improvements may be seen on Figure 60.

(a) Mode 1 History

(b) Mode 2 History

Figure 60: Enforcement Histogram for the first bending mode (mode 1) and the bending torsional mode (mode 2)

6 Flutter Analysis

Every previous analysis served to understand if the connector could cope with the demands of the experiment. All the effort was to ensure that it was the spar element the one governing the flutter and not the rest of the components. Once acceptable stiffness had been achieved a flutter analysis had to be conducted to predict the velocity at which the aeroelastic effects would appear in the wind tunnel research.

6.1 NATRAN Model Update

6.1.1 X-DIA Mass Estimation

The NASTRAN model used to study the flutter (Figure 5) had been simulated with some known masses (the ones associated to the fuselage beam and other already existing components) and some estimated or predicted masses. After the exhaustive design process, many of the components were at a near completion stage and hence would be close to their final versions.

It was previously mentioned that the CATIA suite did not allow to modify the density of the materials beyond the ones it had in its internal database. For this reason, it was the volume of each component that was extracted from the CAD files and then multiplied by its associated density.

The final materials to be used were:

- Aluminium 2011 T3: $\rho = 2823 kg/m^3$
- XT2 Winform: $\rho = 1097 kg/m^3$

Table 14: Aluminium Structural Components

REFERENCE	VOLUME (m^3)	MASS (kg)
fuselage beam	1,079E-03	3,0448
top shell	5,892E-04	1,6633
bottom shell	3,614E-04	1,0202
insert right	1,835E-04	0,5180
insert left	1,835E-04	0,5180
wing spar right	4,548E-04	1,3640
wing spar left	4,548E-04	1,3640
ordinata di forza	1,000E-03	2,8230
vtail connection right	1,831E-04	0,5169
vtail connection left	1,838E-04	0,5189
tail spar	1,948E-04	0,5499
hinge base	3,813E-05	0,1076
hinge	1,669E-05	0,0471
hinge cover	1,388E-05	0,0392
	TOTAL	14,0950

Table 15: 3D XT2 WINFORM Aerodynamics

REFERENCE	VOLUME (m^3)	MASS (kg)
wing sector 1 right	3,8110E-04	0,41807
wing sector 1 left	3,8110E-04	0,41807
wing sector 2 right	3,5100E-04	0,38505
wing sector 2 left	3,5100E-04	0,38505
wing sector 3 right	3,2120E-04	0,35236
wing sector 3 left	3,2120E-04	0,35236
wing sector 4 right	2,9060E-04	0,31879
wing sector 4 left	2,9060E-04	0,31879
wing sector 5 right	3,3830E-04	0,37112
wing sector 5 left	3,3830E-04	0,37112
aileron right	1,6860E-04	0,18495
aileron left	1,6860E-04	0,18495
cover 1 right	4,0110E-05	0,04400
cover 1 left	4,0110E-05	0,04400
cover 2 right	3,6980E-05	0,04057
cover 2 left	3,6980E-05	0,04057
cover 3 right	3,3830E-05	0,03711
cover 3 left	3,3830E-05	0,03711
cover 4 right	3,0650E-05	0,03362
cover 4 left	3,0650E-05	0,03362
cover 5 right	5,3240E-05	0,05840
cover 5 left	5,3240E-05	0,05840
	TOTAL	4,48807

6.1.2 Spar Re-Positioning and Characterization

After the modifications that the "Wing to Fuselage" connection suffered, the wing spar had now shifted its position if compared to the position it initially held in the first flutter analysis. Effectively it had been both translated and rotated, and this changes despite not affecting the natural frequencies, would affect the eigenvectors associated to each mode.

By exploiting the capabilities of 3D rotation matrices and introducing a new reference coordinate system the spar was appropriately positioned in the FEA model. The spar 1D elements were all defined using the same reference system, with respect to which they were all aligned with the local x-axis. So simply by translating the origin of this 5001 ref frame, and adequately rotating it, every other point defined using it would follow the same operations and would automatically be in the correct position.

It is also very important to note that the axis that models the wing spar is the elastic axis, which differs from the geometrical axis that was described in Section 4.1.3. The elastic axis is contained in the same plane as the geometrical axis, but it is positioned 7mm above the spars top plane at the root section and at 6mm above the same plane at tip section as seen on Figure 61.

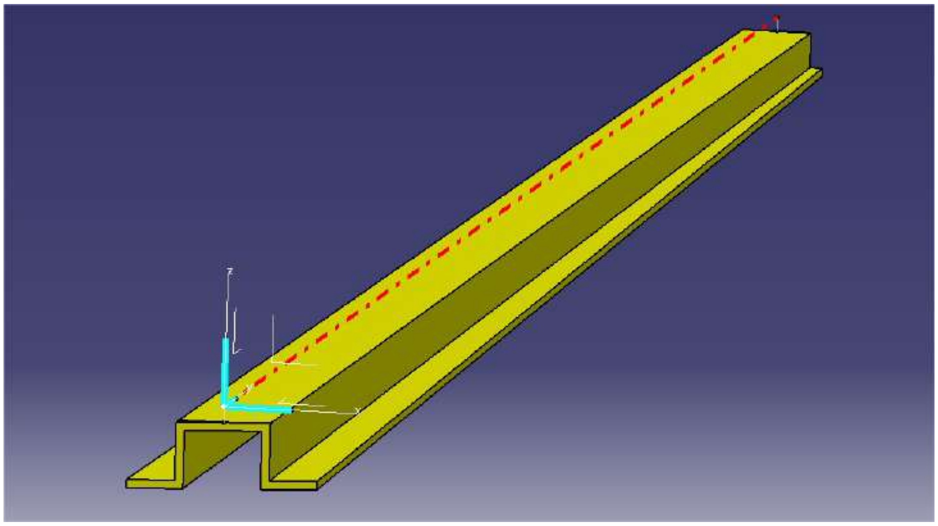

Figure 61: Wing Spar Elastic Axis

NASTRAN's aero-panels, in this case defined as CAERO1 by specifying two leading edge points and the chord at each section, are a simplification of the lifting surfaces and could be interpreted as the midplane of those. From this interpretation it made sense that the modelled wing spar, using

1D elements, should remain out of this plane, as seen on Figure 62c and Figure 62d compared to Figure 62a and Figure 62b.

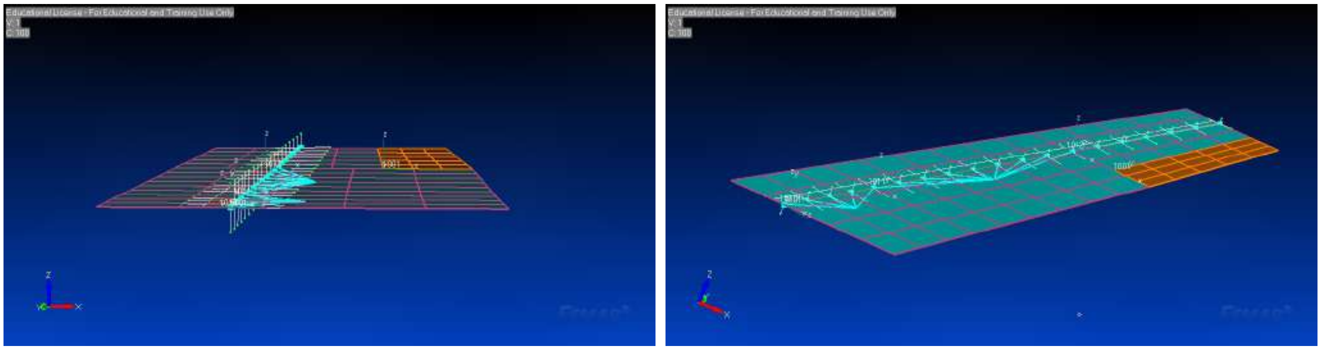

(a) Right View Original Spar Position

(b) Isometric View Original Spar Position

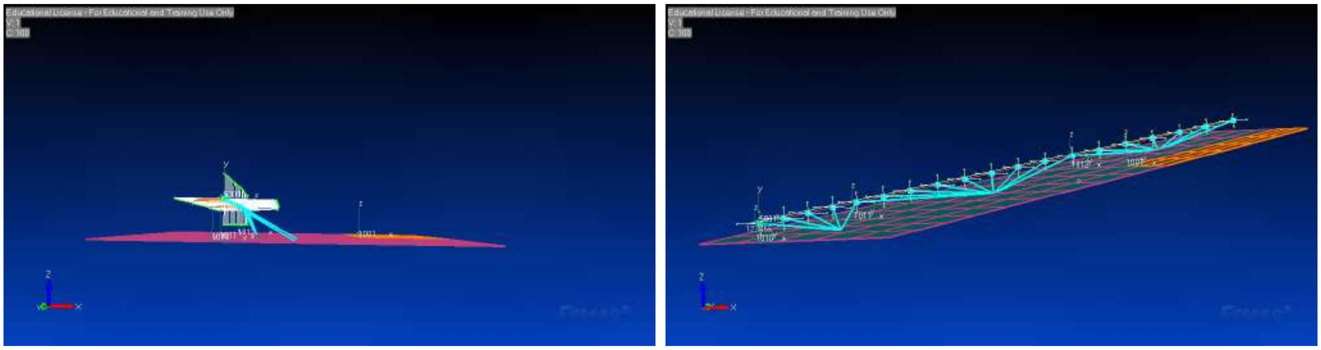

(c) Right View New Spar Position

(d) Isometric View New Spar Position

Figure 62: Comparison of Spar Positioning

The blue lines seen on Figure 62 connecting the spar nodes with the aero-panels are the splines in charge of transmitting the aerodynamic forces into the structural model and vice versa, so they are the glue for the mathematical iteration required to numerically compute the behaviour of the wings as a whole.

Once the spar was positioned, it was necessary to relate the beam spar model with the simulation in Section 5.2. This parametric study was performed to try to represent more accurately the spar-insert interaction. In the original X-DIA NASTRAN model, the spar had already been characterized so this work might seem redundant, but the original representation did not take into account the way in which the insert fitter inside the spar. This fitting effectively shortens the wing spar as already mentioned, making it less compliant and this parametric study had the goal of modelling this structural interaction. For this purpose analysis was run by modifying both Young modulus and Shear modulus to match as closely as possible the ideal case with the simulated constraints. For this analysis, all four modes below 100 Hz were represented so as to chose a configuration that would most truthfully represent the plate simplification of the wing spar.

Table 16: Parametric Analysis for Spar Characterization Under Updated Constraints

E	G	MODE1	MODE2	MODE3	MODE4	DMODE1	DMODE2	DMODE3	DMODE4
7,20E+10	2,75E+10	17,9005	31,0416	63,3538	86,5501	1,71%	4,08%	20,20%	5,26%
7,31E+10		18,0364	31,2116	63,4806	87,2006	0,96%	3,55%	20,04%	4,55%
7,40E+10		18,1468	31,3487	63,5844	87,7292	0,35%	3,13%	19,91%	3,97%
7,50E+10		18,2687	31,4989	63,6999	88,3125	0,31%	2,66%	19,77%	3,34%
7,20E+10	3,00E+10	17,9023	31,3986	65,4431	86,5936	1,70%	2,97%	17,57%	5,22%
7,31E+10		18,0383	31,5768	65,5635	87,2452	0,95%	2,42%	17,42%	4,50%
7,40E+10		18,1487	31,7206	65,6622	87,7745	0,34%	1,98%	17,30%	3,92%
7,50E+10		18,2706	31,8783	65,7719	88,3587	0,33%	1,49%	17,16%	3,28%
7,20E+10	3,50E+10	17,9052	31,9605	69,4749	86,6625	1,68%	1,24%	12,49%	5,14%
7,31E+10		18,0411	32,1520	69,5858	87,3156	0,94%	0,65%	12,36%	4,43%
7,40E+10		18,1517	32,3067	69,6765	87,8462	0,33%	0,17%	12,24%	3,85%
7,50E+10		18,2736	32,4765	69,7773	88,4319	0,34%	0,36%	12,11%	3,20%
7,20E+10	4,00E+10	17,9073	32,3789	73,2999	86,7145	1,67%	0,06%	7,68%	5,08%
7,31E+10		18,0433	32,5804	73,4042	87,3688	0,92%	0,68%	7,55%	4,37%
7,40E+10		18,1539	32,7433	73,4895	87,9003	0,32%	1,18%	7,44%	3,79%
7,50E+10		18,2759	32,9224	73,5841	88,4871	0,35%	1,74%	7,32%	3,14%
7,20E+10	4,50E+10	17,9089	32,7012	76,9340	86,7554	1,66%	1,05%	3,10%	5,04%
7,31E+10		18,0450	32,9106	77,0342	87,4105	0,91%	1,70%	2,97%	4,32%
7,40E+10		18,1556	33,0800	77,1160	87,9428	0,31%	2,22%	2,87%	3,74%
7,50E+10		18,2777	33,2662	77,2066	88,5303	0,36%	2,80%	2,76%	3,10%
7,20E+10	5,00E+10	17,9102	32,9567	80,3933	86,7890	1,65%	1,84%	1,26%	5,00%
7,31E+10		18,0464	33,1722	80,4912	87,4447	0,91%	2,51%	1,38%	4,29%
7,40E+10		18,1570	33,3467	80,5710	87,9775	0,30%	3,05%	1,48%	3,70%
7,50E+10		18,2791	33,5388	80,6593	88,5656	0,37%	3,64%	1,59%	3,06%

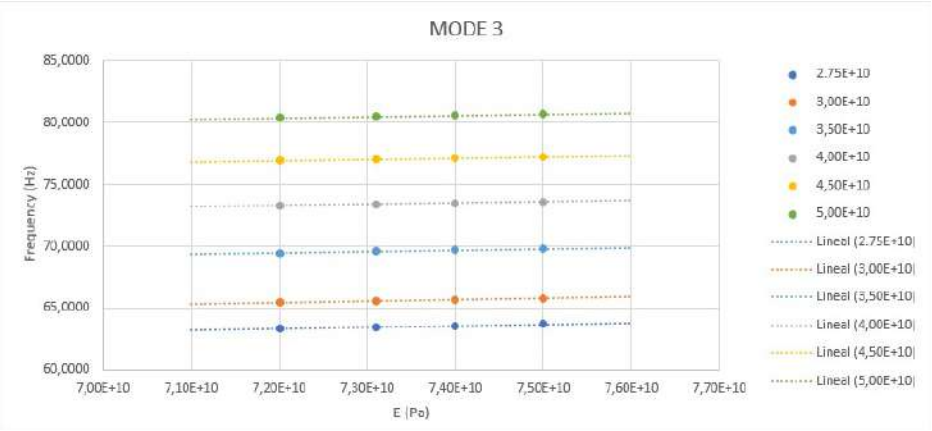

Figure 63: Parametric Analysis Plot of Mode 3 Frequency Versus Young Modulus

The four right most columns in Table 16 are the percentage difference between the modes for any given combination of E and G and the ideal. This columns were then color coded to easily understand the progression with green representing minimum difference while red illustrated biggest deviations from the plate spar model.

In this case due to the spars geometry the relations between E and G were linear as clearly seen in Figure 63, representing the effect of the elastic parameters on Mode 3. This linearity allowed for a simple linear interpolation between values and an optimal E was estimated to be roughly around $7,45E+10$ (Pa). In order to fix the G, it was decided to jump to the case that would most closely match the eigenvalue of mode 3, which is the pure torsional mode of the spar. This decision was taken from the in plane characteristic of the eigenvector associated to mode 2 which would not usually appear in aircraft due to the great stiffness in the wing plane.

Table 17: Representative Structural Parameters for Ideal Spar Behaviour

E (Pa)	G (Pa)	ρ (kg/m^3)	Mode 1 (Hz)	Mode 2 (Hz)	Mode 4 (Hz)	Mode 4 (Hz)
$7,45E+10$	$4,82E+10$	2800	18,2176	33,3527	79,3906	88,2602

6.2 Wing to Fuselage Connector Characterization

Next it was the turn of the "fuselage to wing connector". The advantages of reducing the geometrically complex model to a combination of bar elements has already been illustrated, and following this modus operandi, the connector could be simplified by joining the fuselage beam with the node defining the beginning of the elastic axis in the wing spar. A third node was placed between these other two to increase the discretization of the connector.

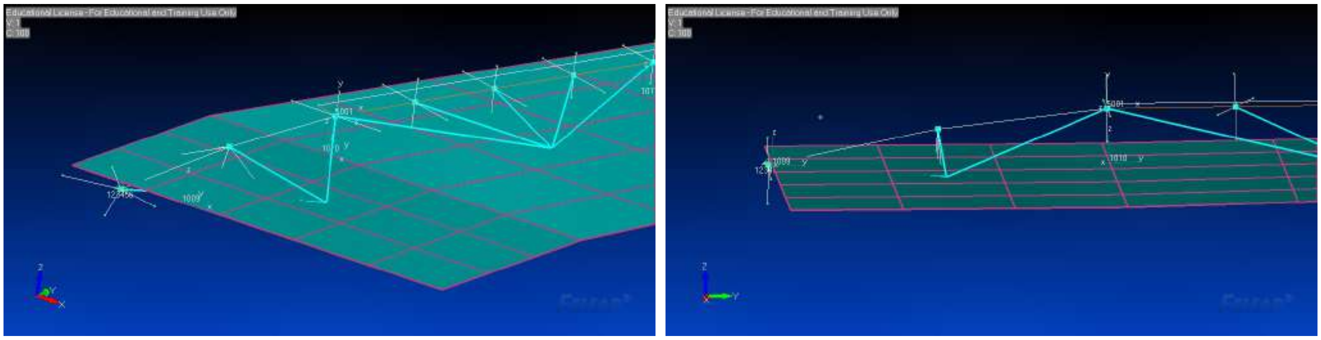

(a) (b)

Figure 64: Modelling of "Wing to Fuselage Connector" by PBAR Elements

Once the required nodes had been defined, a similar process as the one followed in Section 6.1.2 to decide the values in Table 19 was followed. In this case it was not the material properties the ones to modify, but it was the associated beam properties that would have to represent the geometrical peculiarities of the connector itself. Following from one of the previous comments, about the assumed in plane stiffness, the parameters to vary were the associated I2 which represents the moments of inertia in the out of plane rotation and the torsional constant J.

The simplest way to model the mass of the connector was by using lumped masses at 2 different locations. The mass of the shells was introduced at the origin of point where fuselage beam and connector would meet in the FEM model. The insert mass was placed at node where the connector and the spars elastic axis coincided.

Table 18: Parametric Analysis for Wing to Fuselage Connector Characterization

I2	J	MODE1	MODE2	MODE3	MODE4	DMOD1	DMOD2	DMOD3	DMOD4	WEIGHT AVG
9,00E-08	3,00E-08	15,8090	33,3126	74,4443	78,5908	0,22%	25,23%	4,42%	0,10%	8,55%
	5,00E-08	15,9180	33,3270	74,8569	78,8687	0,46%	25,28%	3,89%	0,26%	8,57%
	7,00E-08	15,9654	33,3333	75,0239	79,0076	0,76%	25,30%	3,68%	0,43%	8,68%
	9,00E-08	15,9918	33,3368	75,1136	79,0903	0,93%	25,32%	3,56%	0,54%	8,73%
	1,10E-07	16,0087	33,3390	75,1695	79,1452	1,04%	25,33%	3,49%	0,61%	8,77%
9,50E-08	3,00E-08	15,9000	33,3128	74,8520	78,6067	0,35%	25,23%	3,90%	0,07%	8,50%
	5,00E-08	16,0108	33,3271	75,2913	78,8728	1,05%	25,28%	3,34%	0,26%	8,70%
	7,00E-08	16,0590	33,3334	75,4678	79,0087	1,35%	25,30%	3,11%	0,44%	8,80%
	9,00E-08	16,0859	33,3369	75,5621	79,0906	1,52%	25,32%	2,99%	0,54%	8,86%
	1,10E-07	16,1031	33,3391	75,6207	79,1452	1,63%	25,33%	2,91%	0,61%	8,89%
9,75E-08	3,00E-08	15,9425	33,3128	75,0438	78,6155	0,62%	25,23%	3,65%	0,06%	8,55%
	5,00E-08	16,0542	33,3272	75,4967	78,8750	1,32%	25,28%	3,07%	0,27%	8,75%
	7,00E-08	16,1027	33,3345	75,6780	79,0094	1,63%	25,31%	2,84%	0,44%	8,86%
	9,00E-08	16,1298	33,3370	75,7747	79,0908	1,80%	25,32%	2,72%	0,54%	8,91%
	1,10E-07	16,1471	33,3392	75,8346	79,1452	1,91%	25,33%	2,64%	0,61%	8,95%
1,00E-07	3,00E-08	15,9832	33,3129	75,2281	78,6250	0,87%	25,23%	3,42%	0,05%	8,61%
	5,00E-08	16,0957	33,3273	75,6948	78,8775	1,58%	25,28%	2,82%	0,27%	8,81%
	7,00E-08	16,1445	33,3335	75,8810	79,0101	1,89%	25,31%	2,58%	0,44%	8,91%
	9,00E-08	16,1718	33,3370	75,9800	79,0909	2,07%	25,32%	2,45%	0,54%	8,97%
	1,10E-07	16,1893	33,3393	76,0412	79,1453	2,18%	25,33%	2,37%	0,61%	9,00%
1,10E-07	3,00E-08	16,1297	33,3133	75,8944	78,6705	1,80%	25,23%	2,56%	0,01%	8,80%
	5,00E-08	16,2452	33,3275	76,4201	78,8900	2,53%	25,28%	1,89%	0,29%	9,00%
	7,00E-08	16,2953	33,3337	76,6268	79,0137	2,84%	25,31%	1,62%	0,44%	9,10%
	9,00E-08	16,3234	33,3372	76,7352	79,0918	3,02%	25,32%	1,48%	0,54%	9,16%
	1,10E-07	16,3413	33,3395	76,8016	79,1454	3,13%	25,33%	1,40%	0,61%	9,19%

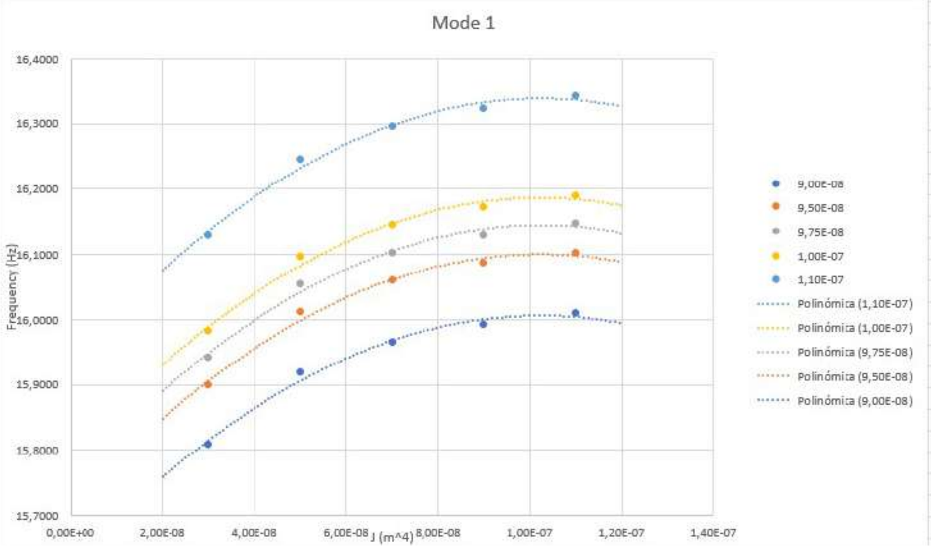

Figure 65: Parametric Analysis Plot of Mode 1 Frequencies vs. Torsional Constant

This time the correlation was non linear as clearly seen in Figure 65 (quadratic trend lines have a good value of R^2 in the vicinity of the desired operating point). Associated to this non-linearity, it was obvious that selecting values to closely match all eigenvalues would be impossible, as there was an imposed maximum for a given I2 after which further increasing the value of J would cause deviation from the desired frequency of mode 1 (the mode that would appear most in the flutter). A possible solution to this problem was to use a combination of I2 and J that minimized a defined deviation weighted average. This average was designed to grant greater importance to the modes that would contribute most to the overall flutter.

Weighted average formula:

$$WAvg_{deviation} = (F_1 * 0.4) + (F_2 * 0.3) + (F_3 * 0.2) + (F_4 * 0.1)$$

Where F_i corresponds to the frequency of the ith natural mode.

Table 19: Representative Structural Parameters for Wing to Fuselage Characterization without Enforcing Plates

I2 (Pa)	J (Pa)	Mode 1 (Hz)	Mode 2 (Hz)	Mode 4 (Hz)	Mode 4 (Hz)
$9,50E-08$	$3,00E-08$	15,9025	33,3128	75,1215	78,6161

6.3 Flutter Analysis Results of the Updated X-DIA

Table 20: Natural Frequencies of First 36 modes.

MODE	FREQUENCY (Hz)	MODE	FREQUENCY (Hz)	MODE	FREQUENCY (Hz)
1	0,0000	13	17,5305	25	63,3281
2	0,0000	14	19,4107	26	65,0493
3	0,0000	15	24,8672	27	70,0364
4	0,0000	16	27,5415	28	70,9340
5	0,0000	17	27,6615	29	75,3658
6	0,0000	18	31,1832	30	78,2622
7	7,9084	19	33,7503	31	79,9745
8	9,6450	20	37,8993	32	81,9534
9	10,7250	21	38,7425	33	83,5776
10	13,0701	22	39,5924	34	85,4031
11	15,3002	23	50,6314	35	86,9356
12	15,6728	24	55,8427	36	92,4399

As seen from the table, the first six modes represent the rigid body motion of the model. From there one we have 3 modes below the 10 Hz bandwidth. This limit value is important because, even though the X-DIA is equipped with advanced servomotors which will operate appropriately up to 15Hz frequencies, the truth is that current actuators mounted on commercial aircraft will work up to a bandwidth of 3Hz. This difference is significant and FAA is prone to work with frequencies up to 10 Hz, in consequence the AFS should regard this value as an upper limit.

Studying the modes in detail it is seen that mode 7 is the equivalent mode to the bending mode of the "Wing to Fuselage Assembly" and that the bending torsional mode seem to be most accurately represented by mode 11.

Now that each mode has been represented, Bode plots are the data that will illustrate if any given mode will cause flutter or not.

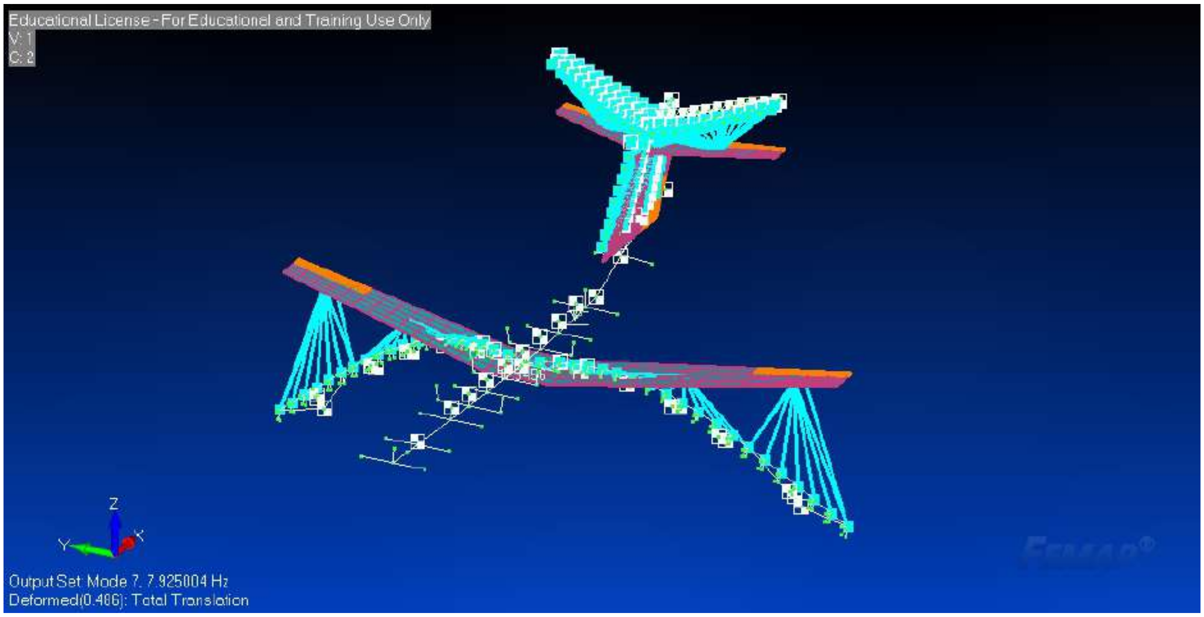

(a)

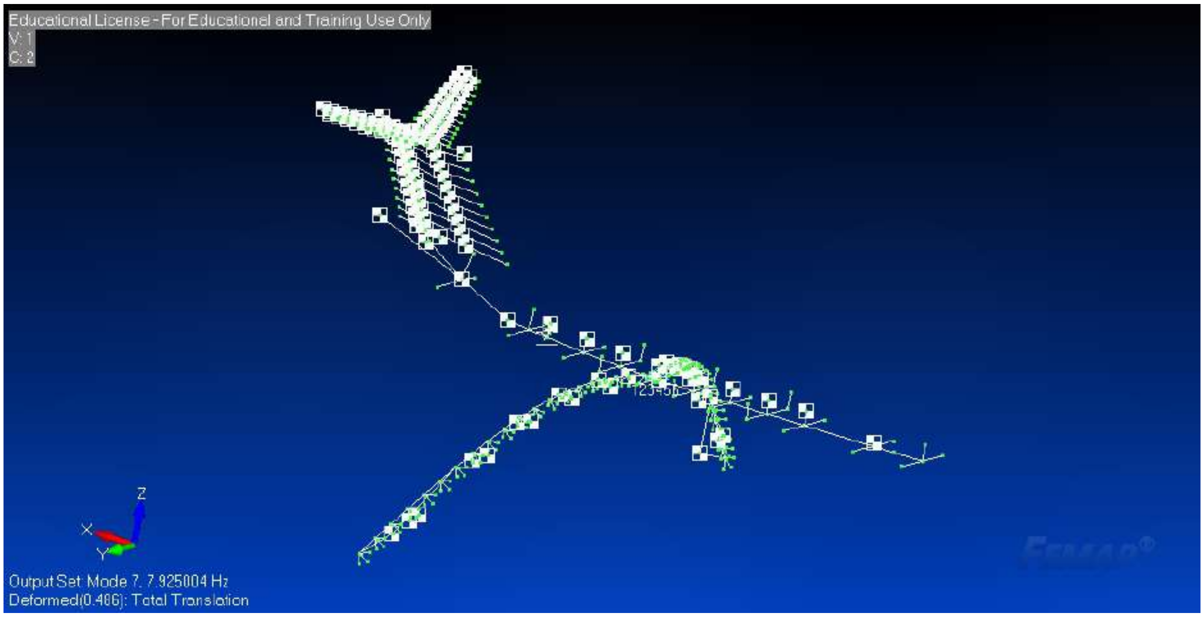

(b)

Figure 66: X-DIA mode 7 equivalent to first bending mode of the wing

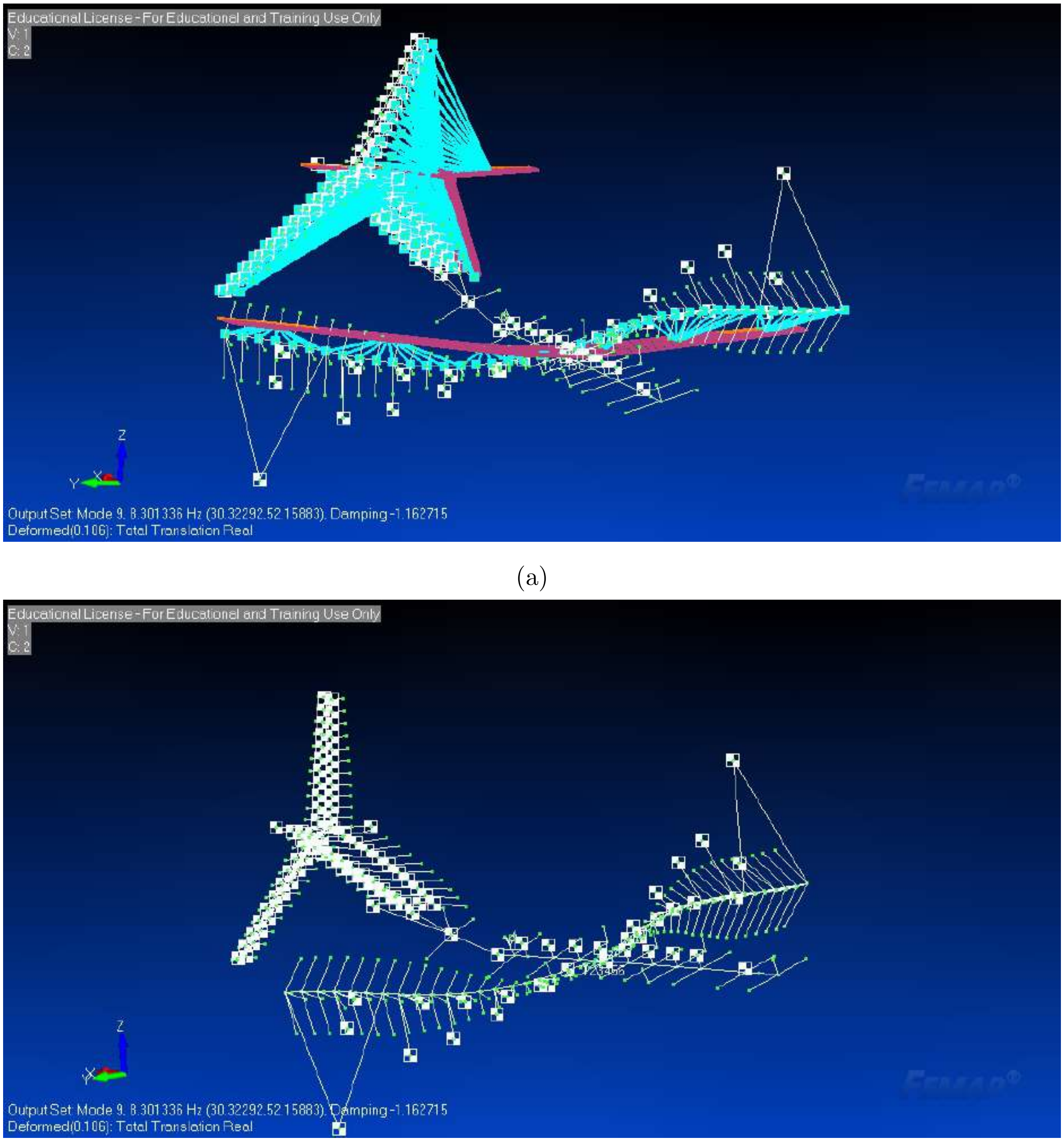
Educational License - For Educational and Training Use Only
V: 1
C: 2

Output Set: Mode 9, 8.301336 Hz (30.32292,52.15883), Damping -1.162715
Deformed(0.106): Total Translation Real

(a)

Educational License - For Educational and Training Use Only
V: 1
C: 2

Output Set: Mode 9, 8.301336 Hz (30.32292,52.15883), Damping -1.162715
Deformed(0.106): Total Translation Real

(b)

Figure 67: X-DIA mode 9 Combination of Anti-symmetric Bending Torsional and Tail Flutter

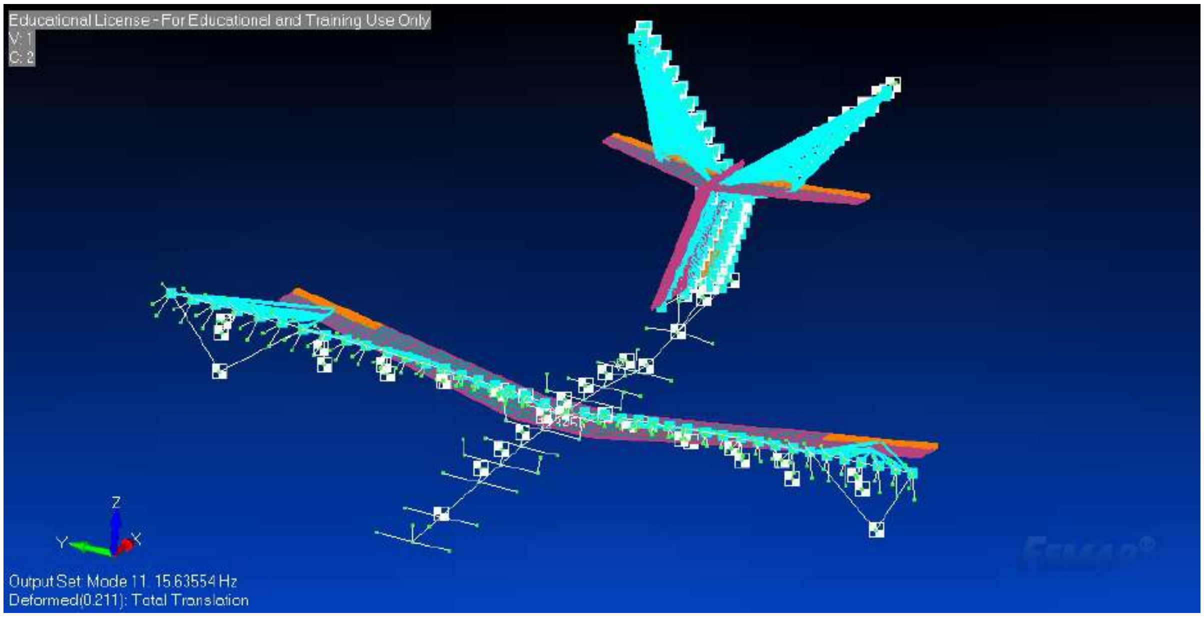

(a)

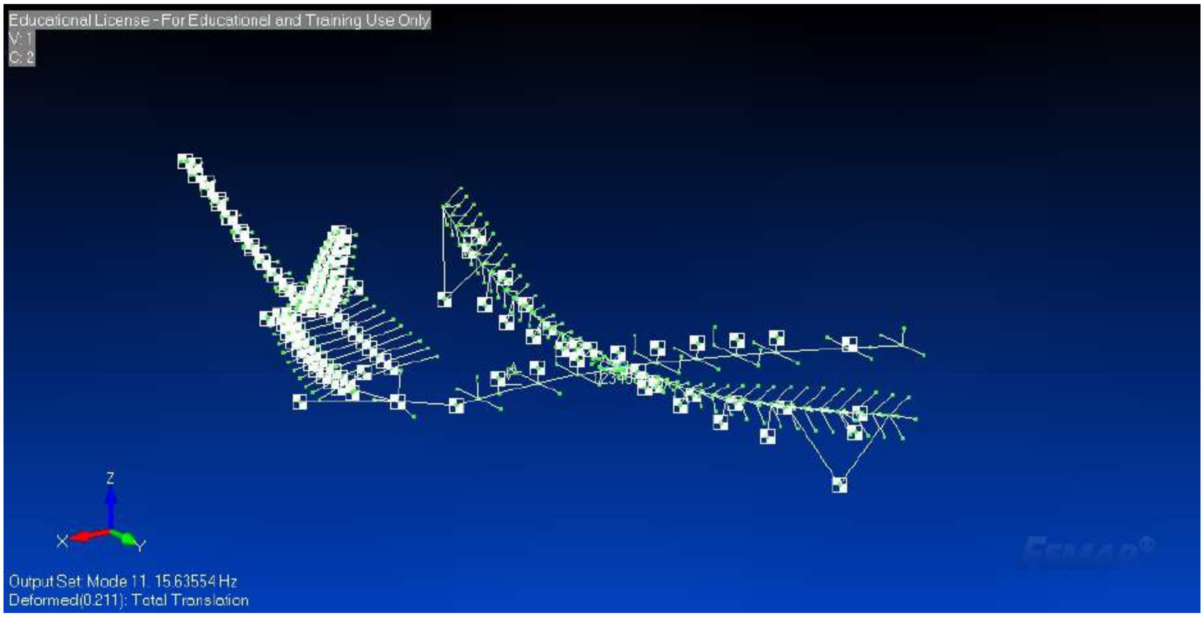

(b)

Figure 68: X-DIA mode 11 equivalent to bending torsional mode of the wing

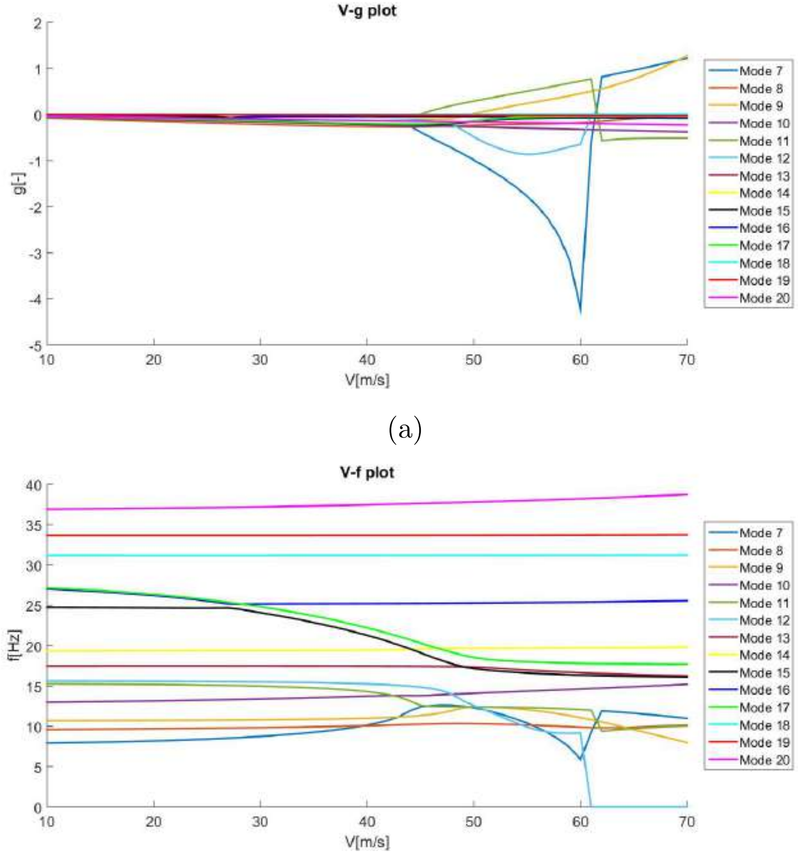

(a)

(b)

Figure 69: Bode Plot of the first 13 modes excluding the rigid motion modes

Looking at the V-g plot, it can be seen that there are 3 modes that enter the diverging region. Precisely the first mode to show flutter characteristics would be mode 11 (bending torsional) which becomes resonant at $V_\infty = 45\ m/s$. As the wind tunnel velocity is increased it should be noted how mode 9 would start to play a role after 50 m/s. Finally while approaching the flutter velocity for mode 7 (bending) with a $V_{flutter} = 62\ m/s$ mode 11 re-enters the damped region.

7 Conclusions

Starting from the requirements the AFS project posed, it was essential to modify the X-DIA's initial configuration. This new architecture had to be easily controllable and manufacturable, so intensive design and optimization was needed to grant the model's performance, if at least just theoretically. The only way to confirm the obtained results would be to validate the structural elements during the experimental sessions, but not making the effort to study and improve the assemblies during the design stage would mean the project was a step closer to failure.

A combination of restrictions lead to the imperative necessity of structurally rigid assembling elements. First of all, flutter velocity had to be attainable at the Large Wind Tunnel facility of Politecnico di Milano. This might lead the reader to think that if there were initial problems to get flutter to manifest below $V_\infty = 55\ m/s$, how come rigidity be the solution instead of compliance. The reader must not forget that the wing spar had been designed with care to obtain the desired flutter characteristics and in consequence any "excessive" compliance on behalf of the assemblies would cause deviation from the ideal behaviour.

Secondly, bandwidth was also a main factor due to FAA's predisposition to certificate AFS controllers working below 10 Hz due to actual controller bounds. Both the new-spar connector interaction and model architecture would have an impact on the frequency of the flutter mode of the full NASTRAN model.

So, recapitulating, the flutter modes that the AFS research project would like to deal with should be as simple and as uncoupled as possible, and for this reason it was interesting to study the how the new mass distribution and the presence of the "Wing to Fuselage Connector" would affect the $V_{flutter}$ and associated eigenvectors.

Related to the connector, the iterative design optimization cycles performed on the assembly allowed to significantly improve it's structural properties, managing to obtain a behaviour with scarce percentage deviation from the spar's ideal modes and modal frequencies. These results, combined with the amended masses were used to update the already existing NASTRAN model and predict flutter modes and velocities.

Finally, from this simulation it is concluded that the $V_{flutter}$ for mode 7 decreases from $69m/s$ to $62m/s$ but is still above the maximum allowable V_∞ , while two new flutter modes (mode 9 & mode 11) appeared. As a consequence the model should be further modified, by load redistribution to obtain flutter velocities below the threshold, making the X-DIA valid for experimentation.

References

[1] MARIO ANDRADES MÁRQUEZ. “Parametric flutter analysis of a wind tunnel conventional aircraft model”. In: (2018).

[2] Jewel B Barlow, William H Rae, and Alan Pope. “Low-speed wind tunnel testing”. In: (1999).

[3] Raymond L Bisplinghoff and Holt Ashley. *Principles of aeroelasticity*. Courier Corporation, 2013.

[4] Sebastiano Fichera and Sergio Ricci. “Freeplay-induced limit-cycle oscillations in a T-tail: numerical vs experimental validation”. In: *Journal of Aircraft* 52.2 (2014), pp. 486–495.

[5] Robert Alexander Frazer, William Jolly Duncan, Arthur Roderich Collar, et al. *Elementary matrices and some applications to dynamics and differential equations*. Vol. 1963. Cambridge University Press Cambridge, 1938.

[6] Eli Livne. “Aircraft active flutter suppression: State of the art and technology maturation needs”. In: *Journal of Aircraft* 55.1 (2017), pp. 410–452.

[7] Jack R Vinson. “Sandwich structures: past, present, and future”. In: *Sandwich structures 7: advancing with sandwich structures and materials*. Springer, 2005, pp. 3–12.

[8] Jan Robert Wright and Jonathan Edward Cooper. *Introduction to aircraft aeroelasticity and loads*. Vol. 20. John Wiley & Sons, 2008.

[9] John H Wykes, MJ Kelpl, and Michael J Brosnan. “Flight test and analyses of the B-1 structural mode control system at supersonic flight conditions”. In: (1983).